Insights into Supercells and Their Environments from Three Decades of Targeted Radiosonde Observations

MICHAEL C. CONIGLIO[a,b] AND MATTHEW D. PARKER[c]

[a] *NOAA/OAR/National Severe Storms Laboratory, University of Oklahoma, Norman, Oklahoma*
[b] *School of Meteorology, University of Oklahoma, Norman, Oklahoma*
[c] *Department of Marine, Earth, and Atmospheric Sciences, North Carolina State University, Raleigh, North Carolina*

(Manuscript received 3 April 2020, in final form 26 August 2020)

ABSTRACT: Hundreds of supercell proximity soundings obtained for field programs over the central United States are analyzed to reconcile differences in recent studies and to refine our knowledge of supercell environments. The large, storm-centric observation-based dataset and high vertical resolution of the sounding data provide an unprecedented look at supercell environments. Not surprisingly, storm-relative environmental helicity (SRH) is found to be larger in tornadic soundings than in nontornadic soundings. The primary finding that departs from previous studies is that storm-relative winds contribute substantially to the larger SRH. Stronger ground-relative winds and more rightward-deviant storm motions contribute to the larger storm-relative winds for the tornadic soundings. Spatial analyses of the soundings reveal lower near-ground pressure perturbations and stronger low- to midlevel cyclonic flow for the tornadic soundings, which suggests stronger mesocyclones, perhaps explaining the more rightward-deviant motions. Differences in the mean critical angle between the tornadic and nontornadic soundings are small and do not contribute to the larger mean SRH, but the tornadic soundings do have fewer instances of smaller (<60°) critical angles. Furthermore, the critical angle is shown to be a function of azimuth from the updraft. Other results include a low-to-the-ground (~250 m on average) hodograph kink for both the tornadic and nontornadic soundings and few notable differences in thermodynamic quantities, except for the expected lower LCLs related to higher RH for the tornadic soundings, somewhat *smaller* 0–3 km lapse rates in tornadic environments related to weaker/shallower capping inversions, and larger 0–3 km CAPE in near-field environments.

SIGNIFICANCE STATEMENT: We analyze hundreds of high-resolution radiosonde observations taken close to supercell thunderstorms during field programs over the last 25 years, resulting in an unprecedented look at supercell environments. There are many results that support, clarify, or refute past hypotheses, but the primary finding that departs from previous studies is that low-level winds relative to the storm are substantially stronger around the time of tornado production compared to nontornadic supercells. These results help to refine our understanding of the conditions that support tornado formation, which provides guidance on environmental cues that can improve the prediction of supercell tornadoes. Future research should explore how to more routinely sample the environments closer to storms to help forecasters better exploit these environmental cues.

KEYWORDS: Atmosphere; Mesocyclones; Severe storms; Storm environments; Supercells; Tornadoes

1. Introduction

Supercells are defined by a quasi-steady rotating updraft (Browning 1964) and are a societal hazard because of their propensity to produce severe weather [hail ≥ 1 in. (2.54 cm), wind gusts ≥ 58 kt (1 kt ≈ 0.51 m s^{-1}), tornadoes] and heavy rainfall. Over the United States, supercells produce the majority of tornadoes (Smith et al. 2012), particularly the significant tornadoes (F/EF2 or greater) that are responsible for a large fraction of injuries and deaths (Brotzge et al. 2013). Improving the forecasting of supercells and tornadoes through understanding of their environments has been a primary focus of the meteorological community for many decades (e.g., Showalter and Fulks 1943; Fawbush and Miller 1954; Rasmussen 2003).

Techniques to predict individual supercell hazards from numerical weather prediction models are promising (e.g., Gallo et al. 2016; Lawson et al. 2018) but forecasters continue to rely heavily on storm–environment relationships to forecast tornadoes (e.g., Coffer et al. 2019, C19 hereafter). It has long been recognized that strong vertical wind shear favors supercells over ordinary thunderstorms (e.g., Fawbush and Miller 1954; Beebe 1958; Newton 1960; Browning and Ludlam 1962). Decades of later research using balloon-borne radiosondes in proximity to supercells highlights the importance of strong low-level vertical wind shear, storm-relative helicity (SRH), conditional instability, and high low-level absolute and relative humidity for tornado production from supercells (e.g., Darkow 1969; Maddox 1976; Brooks et al. 1994; Schaefer and Livingston 1988; Davies and Johns 1993; Kerr and Darkow 1996; Rasmussen and Blanchard 1998; Rasmussen 2003; Craven et al. 2004; Esterheld and Giuliano 2008; Parker 2014, P14 hereafter; Wade et al. 2018, WCZ18 hereafter; Hampshire et al. 2018).

Motivation

Predicting which supercells will be tornadic is still a difficult forecasting problem (Brooks and Correia 2018), so efforts to

Corresponding author: Michael Coniglio, michael.coniglio@noaa.gov

DOI: 10.1175/MWR-D-20-0105.1

better understand their environments through sounding observations should continue. The main problem with this approach is that supercells are relatively rare at any given place and time relative to the nominal twice-daily frequency of soundings. Large distance and time thresholds are needed (see Table 1 of Potvin et al. 2010) to gather enough soundings to make meaningful statistical inferences on supercell–environment relationships. With this wide net comes substantial uncertainty that the sounding represents the environment in which the supercell formed and responds (Maddox 1976; Brooks et al. 1994). An approach to counter this uncertainty is to extract soundings from gridded RUC/RAP hourly model analyses (Benjamin et al. 2016) as proxies for radiosonde observations (e.g., Markowski et al. 2003; Thompson et al. 2003, 2007, 2012; Bunkers et al. 2014; Nowotarski and Jones 2018; C19). While useful storm-environment relationships can be obtained from the RUC/RAP profiles (Thompson et al. 2007; Coniglio 2012), questions remain on their accuracy. For example, Thompson et al. (2003) found RUC soundings to be too cool and dry near the surface. WCZ18 found RAP soundings to be too warm and dry near the surface, enough so to prevent their use in identifying differences in tornadic versus nontornadic subsets. C19 suggested that a lack of a difference in low-level lapse rates and CAPE between the significantly tornadic and nontornadic cases in their dataset could be related to RAP temperature biases.

Another problem with using both observed and RUC/RAP analysis soundings is the limited vertical resolution. Variables from RUC/RAP soundings are customarily interpolated to 25 hPa levels prior to analysis, and while radiosonde systems record data at 1–2 Hz, researchers usually use the processed soundings that typically have only 50–100 points throughout the troposphere (Ingleby et al. 2016). These thinned observations and analyses may miss important details in the vertical profiles. For example, C19 suggested that SRH computed over the lowest 250 m may best discriminate tornadic and nontornadic supercells but urged caution because this computation from RAP profiles only included one point above ground.

Radiosonde observations obtained for field programs can ameliorate errors from representativeness and low resolution by targeting phenomenon and producing a factor-of-10 (sometimes far more) points than the coded observations in standard operational data (Ingleby et al. 2016). Indeed, field-program proximity soundings analyzed by P14 and WCZ18 show features not seen before in supercell composite soundings, but these two studies are not in complete agreement. A goal of this study is to reconcile inconsistencies between P14 and WCZ18 with a large dataset of near-supercell soundings obtained from field programs over the last three decades. Although the initial impetus for this paper came from questions raised by P14 and WCZ18, we also have the broader goal of refining our understanding of supercells and their environments.[1]

TABLE 1. Summary of the differences in analysis techniques between P14, WCZ18, and this study.

	P14	WCZ18	This study
No. of quality-controlled soundings	134	28 far-field–near-field pairs (56 total)	Up to 902 (varies by subset and analysis)
Min. No. of soundings per storm	7	2	1
No. of supercells	12	19	Up to 216 (varies by subset and analysis)
No. of tornadic vs nontornadic supercells	7 tornadic (1 F/EF2+), 5 nontornadic	9 tornadic (5 F/EF2+), 10 nontornadic	112 tornadic (39 F/EF2+), 108 nontornadic
No. of days	11	15	110
Max. proximity distance	~100 km	~90 km	120 km (100 km for subsets, 300 km for gridded analysis)
Proximity time	After storm initiation and before storm demise	As in P14	As in P14
Analysis methods	3D gridded composite of sounding perturbations from the background environment, then extraction of vertical columns recentered on the mean base-state sounding to compute sounding variables	Mean vertical profiles of the soundings and a comparison of near-field vs far-field differences and their distributions	A more traditional approach of comparing mean vertical profiles (soundings and hodographs) and a gridded composite of sounding variables computed from individual soundings

[1] Another goal is to evaluate the RUC/RAP-based analyses developed by SPC that are routinely used for defining the environment of storms in a wide variety of applications (e.g., Thompson et al. 2012; Hart and Cohen 2016; C19), but this particular analysis will be presented in a later companion paper.

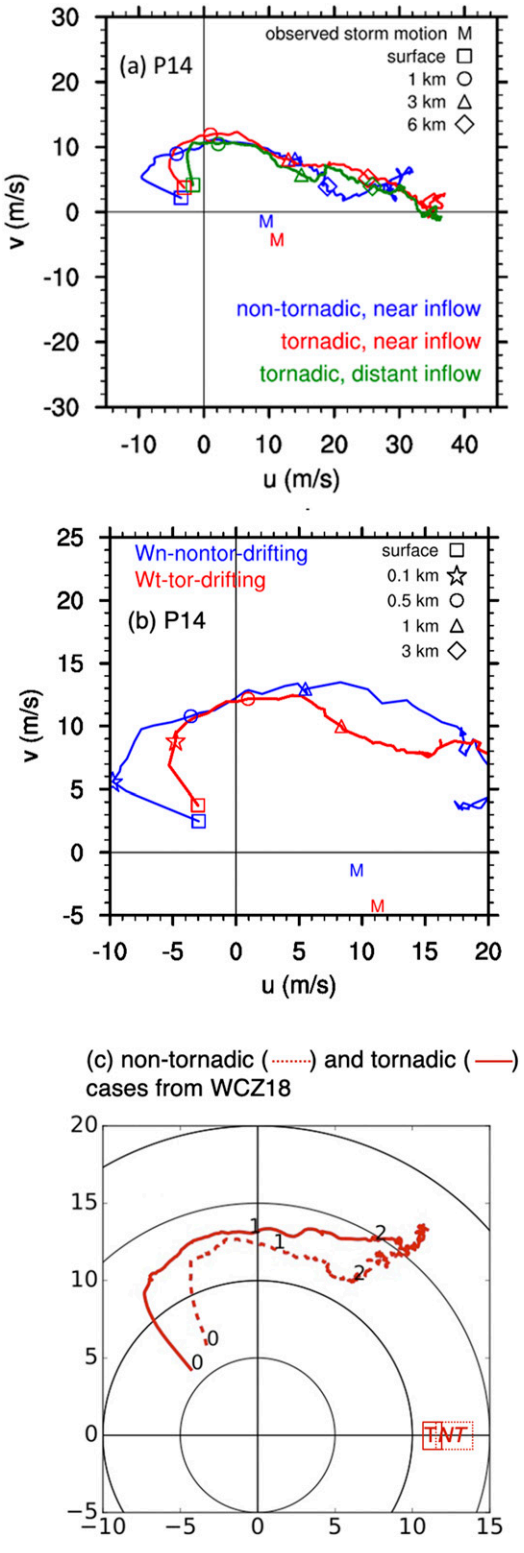

FIG. 1. (a) Composite hodograph from P14 showing tornadic gridpoint profiles 80 (green) and 40 km (''near inflow'') southeast of the updraft for the tornadic (red) and nontornadic (blue) gridpoint profiles. The surface, 1, 3, and 6 km data points are denoted with symbols as shown. (b) Composite hodograph from the P14 analysis resampled at the mean locations of the near-inflow soundings from WCZ18 (Wn: nontornadic; Wt: tornadic). The surface, 0.1, 0.5, 1, and 3 km data points are denoted with symbols as shown. In (a) and (b) the observed mean storm motion is plotted with ''M.'' (c) Mean near-inflow profiles for the tornadic (solid line) and nontornadic (dashed line) soundings from WCZ18. Storm motion in (c) is along the x axis with a mean speed 11.6 m s^{-1} for the tornadic soundings (T) and 12.8 m s^{-1} for the tornadic soundings (NT). Numbers on the hodograph denote height AGL in km.

2. P14 and WCZ18 studies

P14 produced a comprehensive composite sounding analysis of the well-sampled storms from VORTEX2. To address the goal of observing near-storm inflow modification, WCZ18 analyzed pairs of nearly simultaneous sounding observations taken in the inflow of supercells with one member of each pair typically being 20–30 km closer to the storm than its counterpart. Not surprisingly, given the use of different methods, cases, and numbers of soundings per case (summarized in Table 1), the WCZ18 results differed somewhat from those of P14. There were subtle differences in the low-level temperature and moisture profiles, but of most interest to this study, WCZ18 showed much more near–ground streamwise horizontal vorticity in the environments of nontornadic supercells than those in P14 resulting from a different ''critical angle''—the angle between the near-ground storm-relative inflow and low-level wind shear vectors (Esterheld and Giuliano 2008) (Fig. 1). Furthermore, in WCZ18 the nontornadic mean hodograph changed little with distance from the storm, whereas the mean hodograph became larger closer to tornadic storms. The opposite was true in P14. The distinctions between the conclusions of these studies could be relevant operationally and for interpretations of modeling studies that use the P14 composites for initial conditions (e.g., Coffer and Parker 2018).

Balloon drift, which P14 takes into account but WCZ18 does not, is likely not the reason for these differences. Comparisons of vertical profiles extracted from the P14 analyses that include and do not include the sondes' horizontal displacement with height showed very little difference. Among many combinations explored, Fig. 2 depicts one of the largest differences found. As the sonde approaches the storm in midlevels, the storm-relative winds are somewhat stronger and the humidity is somewhat higher. Notably, however, the thermodynamic and wind profiles in the lowest 1–2 km AGL are nearly identical.

It is important to consider the location of the environmental soundings relative to the storm because considerable spatial variability can be present in the inflow sector of supercells (Markowski et al. 1998; Potvin et al. 2010; P14; WCZ18). The nontornadic hodographs differ the most between P14 and WCZ18 (Fig. 1), and indeed the mean location of the nontornadic soundings are different, whereas the mean location of the tornadic soundings are nearly the same (Fig. 3). To explore the impact of these different updraft-relative sounding

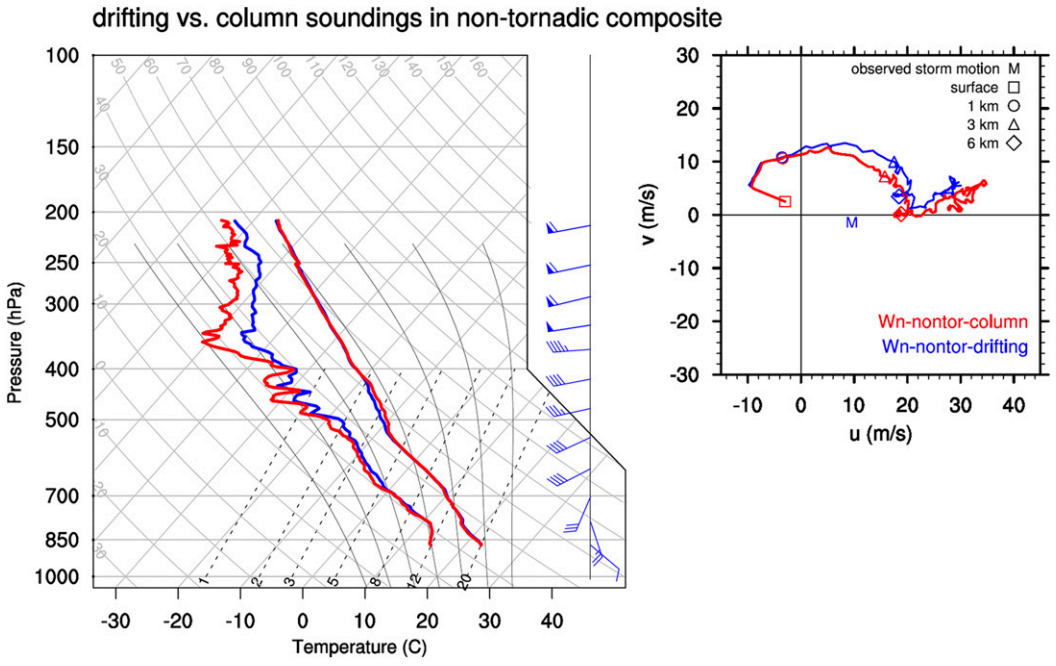

FIG. 2. (left) Skew T–log$p$ thermodynamic diagram and (right) hodograph for profiles begun at the WCZ18 nontornadic near-inflow location ("Wn" in Fig. 3), for both a purely vertical column (red) and a pseudo-drifting sonde (blue), within the nontornadic subset composite analysis of P14. On the hodographs, the surface, 1, 3, and 6 km data points are denoted with symbols as shown, with the observed mean storm motion plotted with "M." For reference, the vertical wind profile associated with the drifting sonde hodograph is plotted atop the skew T–log$p$ diagram (half barb = 2.5 m s^{-1}, barb = 5 m s^{-1}, flag = 25 m s^{-1}).

locations, the P14 3D composite was resampled at multiple storm-relative locations. Indeed, differences in the low–level wind profile emerge solely from differences in the launch location (Fig. 4). For the P14 tornadic soundings, locations closer to the eventual storm path show lower tropospheric winds that are more backed, which corresponds to the tendency for a near-storm pressure minimum to accelerate inflow toward the storm from all directions. Interestingly, as shown in Fig. 4c, the nontornadic P14 soundings show little difference in winds below 500 m as a function of azimuth, but do show differences as a function of range (the differences in tornadic soundings as a function of range in P14 can be seen in Fig. 1a). Although sampling differences between P14 and WCZ18 likely contribute to more backed near-surface winds for the nontornadic soundings in P14 compared to WCZ18, these differences in storm-relative location could explain some of the more veered (less easterly and more southerly) near-surface winds in the nontornadic composite in WCZ18 (dashed red line in Fig. 1c) compared to the tornadic composite in WCZ18 (solid red line in Fig. 1c) and the nontornadic composite shown in P14 (blue line in Fig. 1a). This also provides motivation for future researchers to pay attention to the possible impacts of storm-relative position upon the environments depicted in their sounding datasets. Ultimately, the limited sample sizes of storms in P14 and WCZ18 (Table 1) prevents a more thorough exploration into the differences shown above, which provides the motivation for this study to compile and analyze a much larger dataset of supercell proximity soundings.

3. Data collection, processing, and analysis methods

Most of the radiosonde observations for this study were collected from the NCAR Earth Observing Laboratory (EOL) field project data archive with some obtained from the Atmospheric Radiation Measurement (ARM) data archive or directly by the lead author. To maintain some geographical and seasonal consistency among the soundings, only those obtained from the central United States in the spring and early summer are used here (spanning mid-April to mid-July). Soundings taken within ~160 km of a supercell updraft were collected from selected field projects dating back to 1994 (Table 2) and were assigned to the closest supercell at the time the sonde was released (or close to the ground for dropsondes).

Candidate supercells sampled by at least one sounding were first identified using NCEI composite reflectivity observations, and later scrutinized manually using Level II data from the closest WSR-88D radar to ensure supercell characteristics (hook echo, bounded weak echo region, or mesocyclone) lasted for at least 60 min. Using WSR-88D Level II data viewed within the NCEI Weather and Climate Toolkit, the latitude and longitude of the supercell updraft was recorded manually at every volume time (~ every 5.5 min) from first echo to when the supercell could no longer be tracked (from dissipation, upscale growth, or a merger with other storms). The updraft location was

determined subjectively using the location of the inflow notch adjacent to a hook echo on base scan reflectivity, weak echo regions aloft, and/or mesocyclone on radial velocity observations as guidance. For instances when none of these features could be determined (uncommon for mature storms), a location on the low-level upwind edge of the echo is used as the updraft location. This had to be done in the several volume scans after the first echo but prior to the presence of clear supercell characteristics in the storm. While many of the storms were isolated and straightforward to track, there were also some that were close to other storms making updraft identification more difficult. If a weak echo region aloft, hook echo, or mesocyclone could no longer be detected after interference with nearby storms, the storm in question was no longer tracked. Finally, unlike for some past datasets (e.g., Markowski et al. 2003; Thompson et al. 2003), no minimum threshold for azimuthal shear was used, but the other radar characteristics were required to persist for 60 min rather than the 30 min used in those studies.

The motion of each supercell at each volume time was determined in two steps: first, a five-point (20–25 min) weighted average of instantaneous storm-motion components (using weights of 0.05, 0.2, 0.5, 0.2, and 0.05) was computed. The instantaneous storm motions were based on the bearing and great circle distance between successive latitude and longitude points assigned to the updraft. Then, the three storm-motion components succeeding the sounding time are averaged to obtain the final storm-motion estimate at the time of the sounding, so 30–35 min of instantaneous storm-motion components influence the average. This method differs somewhat from that used in past studies. For example, in Markowski et al. (2003) and Thompson et al. (2003) storm motions are 30–60 min averages of the echo centroid motion using composite radar imagery available at the time (R. Thompson 2020, personal communication). In Bunkers et al. (2000, 2014), most supercell motions were calculated (i) by tracking the centroid of the supercell, (ii) during the most intense phase of the supercell (or when it was tornadic), (iii) averaging over a ~60 min period, and (iv) when the supercell was separated from other storms by several tens of kilometers (Bunkers et al. 2000). Given the subjectivity involved it is impossible to compare these methods to ours exactly; however, we obtained the datasets used in those studies and 19 comparisons can be made from 17 separate supercells that were common to all of our studies. Figure 5a shows that most (16 out of 19) differences in the storm motion vectors have magnitudes $\leq 5\,\mathrm{m\,s^{-1}}$. However, on average the estimates used in the present study tend to be more clockwise than those used in those past studies—the mean and median of the v component difference is about $-1.6\,\mathrm{m\,s^{-1}}$. Some of this difference could be related to our use of a weighted average and our shorter smoothing period as shown by storm motion vectors that turn counterclockwise as longer periods influence the average (Fig. 5a); however, the averages up to 120 min still reside to the right of the average motion vector from the past studies (black arrow in Fig. 5). This indicates other factors are likely present, perhaps relating to different times used in the supercell life cycle (Bunkers et al. (2000, 2014) allowed for ±3 h from the sounding time). The above analysis shows that *the method to compute storm motion performed here appears to identify temporary rightward-deviant motions that often precede tornadoes* that may not be represented in those past studies. This is illustrated in Figs. 5b–d for the three cases that have the largest storm-motion differences shown in Fig. 5a. The identification of these occasional rightward jogs has implications for interpreting storm-relative quantities as described later.

Over 1000 soundings were compiled but the number was reduced to 902 after quality control (QC). Most of the soundings were already QC'ed extensively by EOL (as in Ciesielski et al. 2012), but each sounding was inspected manually by the first author using skew T–log$p$ diagrams and hodographs as guidance to determine if additional QC was needed. Given our focus on details of the low-level wind profile, particular care was given to removing suspect near-ground wind observations.[2] Wind observations were removed most often because of large discrepancies in wind directions (e.g., >30°) between the surface[3] and the level immediately above, and from unrealistically high wind speeds (e.g., $>50\,\mathrm{m\,s^{-1}}$) seen in the first few levels above the ground, most often seen in the VORTEX1 soundings.

For thermodynamic observations, suspect temperature and humidity observations were most often removed because of large temperature lapse rates near the ground (e.g., temperature decreasing >4 K from the surface to 20 m) and large lapse rates that can occur as the sonde rises out of clouds. Furthermore, the recorded altitude of the sounding occasionally needed adjusting (again, the majority from VORTEX1) based on notes provided in the metadata or from cross checks with the latitude and longitude of the sonde. A dry bias of Vaisala RS80 sondes used in VORTEX1 and by ARM-SGP in 1996–98 was addressed by increasing the RH as a function of height based on the mean dry-bias correction derived from Fig. 13 of Wang et al. (2002). Finally, a sounding was flagged if it clearly sampled low-level storm outflow based on manual inspection of the temperature and humidity in the sounding.

Before compositing, winds were rotated to coordinates with the storm motion direction aligned with the x axis and then translated with the storm motion at the origin. All variables were linearly interpolated to common levels every 10 m AGL. To preserve high vertical resolution, an input data point was required to be within 50 m of a common level; otherwise the output data were set to missing. Finally, small-scale noise in the composite fields in each scalar and wind component was removed by fitting an approximating cubic spline using NCL version 6.6.1 (UCAR/NCAR/CISL/TDD 2019) with missing input data returned to the final profile to preserve high resolution.[4]

[2] Many of the soundings impacted by this additional QC were from VORTEX1 that used the NCAR Cross-Chain LORAN Atmospheric Sounding System (Rust et al. 1990). Near storms, signal reception for the LORAN-C navigation system (Passi and Morel 1987) was not as reliable as the modern GPS-based systems (Rust et al. 1999).

[3] Hereafter, the lowest reported level of the sounding—usually below 10 m—will be referred to as the surface.

[4] Application of this interpolating spline also was necessary to remove pendulum oscillations of the sonde in the wind profile from the TELEX and miniMPEX soundings (details and impacts of this spline method can be found in WCZ18). This oscillation was removed with either the proprietary Vaisala algorithm or by the EOL QC procedure for the other field project data.

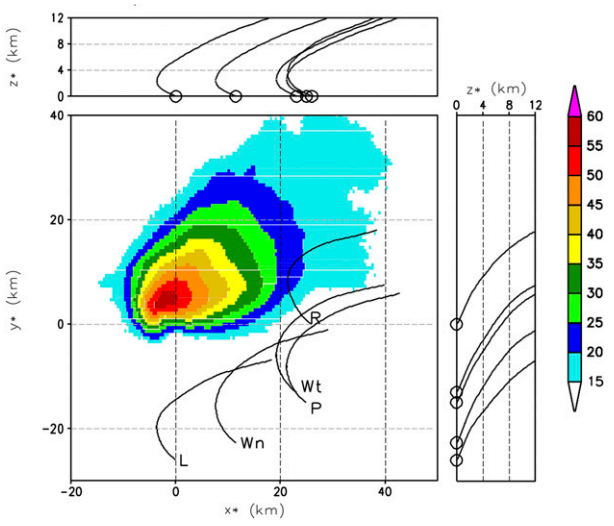

FIG. 3. Trajectories for pseudo-drifting sondes from the five launch points discussed in section 2, projected onto three Cartesian planes (as described in P14); (bottom left) x^*–y^* plan view plot, (top left) x^*–z^* cross-sectional plot, and (bottom right) y^*–z^* cross-sectional plot. All of the positions are storm relative (with the composite storm updraft position at $x^* = 0$ km, $y^* = 0$ km). The averaged base scan radar reflectivity for all supercells from P14 is shaded on the plan view chart. As described in the text, the launch points are labeled "P" for the P14 tornadic and nontornadic near–inflow point, "Wt" for the WCZ18 tornadic near-inflow point, "Wn" for the WCZ18 nontornadic near-inflow point, and "L" and "R" for the hypothetical leftmost and rightmost near-inflow points.

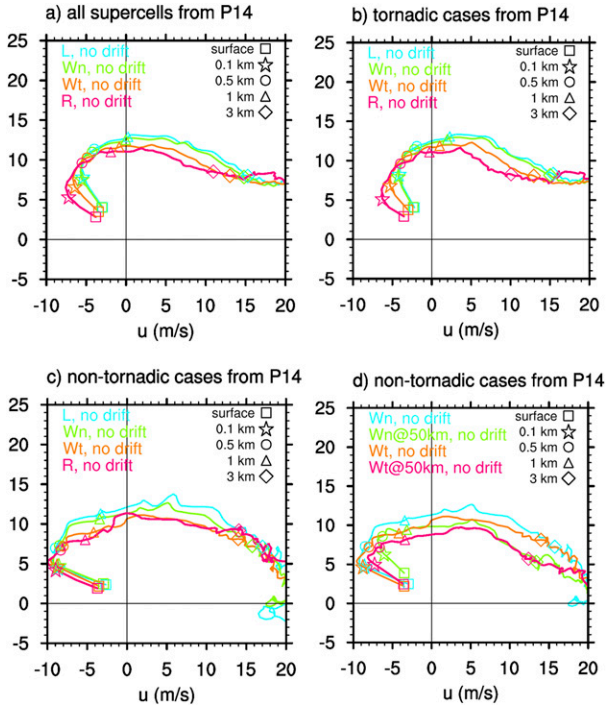

FIG. 4. Composite hodographs from P14 for gridpoint profiles at the "L," "Wn," "Wt," and "R" locations shown in Fig. 3 for (a) all supercells, (b) tornadic supercells, and (c) nontornadic supercells. These locations are about 26 km from the updraft to match the mean near-field sounding location from WCZ18. (d) Composite hodographs for the nontornadic supercells at the "Wt" and "Wn" locations, as well as at locations 50 km from the updraft along radials that pass through "Wn" and "Wt." On all hodographs the surface, 0.1, 0.5, 1, and 3 km data points are denoted with symbols as shown in the legend.

The presence of (or lack of) a tornado and its F/EF-scale rating at each point along each supercell track was determined using the SPC Severe Weather Database files and cross checked with comments made in NWS Storm Data and with WSR-88D Level II data to verify the time and location of the tornado. A sounding was labeled tornadic (torcat = F/EF-scale rating) if there was a tornado occurring with the assigned storm at any time within 6 min prior to and 90 min after the sonde was near the ground (launch time for upsondes, crash time for dropsondes). The sensitivity of the results to other reasonable choices for time windows (e.g., 0 to 60 min or −15 to 75 min) is very small. Two categories of nontornadic soundings were created: if the supercell was never tornadic (torcat = −2) and if the supercell was tornadic outside of the time window of the sounding as described above (torcat = −1). Figure 6 shows the storm-relative near-ground location of the 902 QC'ed soundings along with their assigned tornado category. The tracks of the 216 supercells sampled by the 902 soundings, and the tornadic portions of the tracks, are shown in Fig. 7. The 216 supercells were sampled over 109 unique days. On 12 of those days there were tornadic and nontornadic supercells ongoing at the same time within 120 km of each other (as in Klees et al. 2016). As for the other days, the sounding is assigned to the storm that was closest to the location of the sonde at launch or crash time.

Numerous comparisons of variables (Table 3) and mean soundings/hodographs between two subsets are made with statistical significance in subset-mean differences assessed through a two-tailed t test assuming unequal variance (Welsh's t test) at four significance levels (75%, 90%, 95%, 99%). Given the relatively large number of soundings composited in each subset, the variable distributions do not stray far from Gaussian, which justifies the use of the parametric t test. The number of individual storms sampled, not the number of soundings in each subset, is used as the effective sample size (degrees of freedom) as many soundings were obtained in close proximity in space and time and are likely not independent.

For the sounding and hodograph composites, numerous distance and azimuth thresholds for defining proximity to the updraft were tested, but results focus on soundings gathered within 120 km of the updraft and within −130° to 40° azimuth using the convention shown in Fig. 6. Furthermore, we require 0–3 km CAPE >0, which removes soundings not flagged as outflow that still may have sampled an air mass unfavorable for convection (e.g., on the west side of a dryline or behind a cold front). For all of the comparisons shown, the nontornadic subset comprises the soundings that sampled a supercell that was never tornadic (torcat = −2). Using these subsets and the criteria above, 240 nontornadic soundings remain that sampled

TABLE 2. Summary of the field projects and data sources of the 902 quality-controlled soundings used for this study. The number of dropsondes used from IHOP and BAMEX are indicated in parentheses. Data period is for the processed field project observations from the various sources, but NWS soundings at 6 s data periods in the EOL finalized composite datasets from VORTEX1, BAMEX, VORTEX2, MPEX, and PECAN and are also used here. The approximate vertical spacing of the data points can be obtained by multiplying the data period by the nominal ascent (descent) rate of 5 (10) m s^{-1}.

Project/source	Meaning	Year(s)	No. of soundings	Data period (s)
VORTEX1	Verification of the Origins of Rotation in Tornadoes Experiment	1994–95	167	10
ARM–SGP	Atmospheric Radiation Measurement–Southern Great Plains	1996,1998	18	2
STEPS	Severe Thunderstorm Electrification and Precipitation Study	2000	1	1
IHOP	International H_2O Project	2002	24 (12 drop)	1
BAMEX	Bow Echo and Mesoscale Convective Vortex Experiment	2003	33 (22 drop)	1
TELEX	Thunderstorm Electrification and Lightning Experiment	2004	19	1
VORTEX2	Second Verification of the Origins of Rotation in Tornadoes Experiment	2009–10	313	1
MC3E	The Midlatitude Continental Convective Cloud Experiment	2011	9	2
DC3	Deep Convective Clouds and Chemistry Project	2012	8	1
MPEX	Mesoscale Predictability Experiment	2013	129	1
PECAN	Plains Elevated Convection at Night	2015	42	1
mini–MPEX	mini Mesoscale Predictability Experiment (Coniglio et al. 2019)	2016–17	61	1
TORUS	Targeted Observations using Radars and Unmanned Aircraft Systems of Supercells	2019	52	1

92 supercells over 66 days, and 190 tornadic soundings remain that sampled 75 supercells over 55 days (see Table 4 for an accounting of how the 902 total soundings are reduced to 430 for the main comparison). Note that there was no time-of-day criteria used, and so the UTC times of the soundings range from 1733 to 0639 UTC, but the large majority of the soundings (90%) were released before 0200 UTC. Differences in the UTC time distributions between the two subsets are small (not shown) and are negligible in that they are not found to impact any of the interpretations that follow. The numbers of soundings, storms, and days for all the sounding comparisons discussed next are shown in Table 5 and provided in the upper-left corner of the skew T–log$p$ diagrams.

4. Composite analyses

Presented first is a comparison of the mean 240 nontornadic and 190 tornadic soundings (Fig. 8). As expected, the mean MLLCL and MLCIN are lower (in an absolute sense) for the tornadic subset related to higher low-level humidity. The tornadic subset has somewhat larger mean 0–3 km CAPE and a significantly *smaller* mean 0–3 km lapse rate related to a layer above the boundary layer that is slightly warmer (coming mainly from stronger capping inversions in the far-field tornadic soundings as shown later). This latter result supports the conclusion of C19 that low-level lapse rates are typically not larger in tornadic supercell environments, at least for the central U.S. events represented here (this may not apply to regions like the Southeast United States that experience a larger frequency of high-shear/low-CAPE supercells; e.g., Sherburn et al. 2016). The lack of a signal for larger low-level lapse rates differs from Hampshire et al. (2018) who found significantly larger low-level lapse rates in violent tornado environments (restricting our dataset to tornadoes rated F/EF2 and stronger does not change our results as shown later). The reasons for this difference are not clear but could be related to less restrictive criteria for proximity soundings used in Hampshire et al. (2018) as well as a smaller sample size.

Not surprisingly, the mean SRH is larger (at the 90% significance level or higher) for the tornadic subset for every layer examined (Fig. 8). The direct role of SRH in mesocyclone intensity and dynamic lifting that may support tornadogenesis is well established (Davies-Jones 1984; Markowski and Richardson 2014; Coffer and Parker 2017). SRH is defined as

$$\mathrm{SRH} = \int_{z_1}^{z_2} (\mathbf{V} - \mathbf{C}) \cdot (\nabla \times \mathbf{V})\, dz, \tag{1}$$

where $\mathbf{C}$ is the storm-motion vector, $\mathbf{V}$ is the horizontal wind vector, and the integrand $(\mathbf{V} - \mathbf{C}) \cdot (\nabla \times \mathbf{V})$ can be written as $|\mathbf{V} - \mathbf{C}| \times |\partial \mathbf{V}/\partial z| \times \sin\theta$, the product of the magnitude of the storm-relative wind, the magnitude of the vertical wind shear, and the sine of the critical angle (θ). As discussed in section 2, θ differs substantially for the nontornadic soundings in P14 and WCZ18, which leads to differing conclusions on the importance of near-ground SRH in discriminating tornadic and nontornadic supercells. Esterheld and Giuliano (2008) use the 10 m storm-relative wind and the 0–500 m shear vector to compute θ. Here, we compute θ using the 10 m storm-relative wind and the shear vector over the lowest 100, 250, and 500 m (these layers are referred to collectively as ''near-ground'' hereafter). Figure 8 suggests that both the P14 and WCZ18 results showing differing critical angles between tornadic and nontornadic storms may not be general. In this study, there is very little difference in the orientation of the mean vertical wind shear[5] below 500 m, which results in remarkably similar

[5] The magnitude of the vector difference between two layers, or the bulk wind difference, is used here as a proxy for vertical wind shear magnitude.

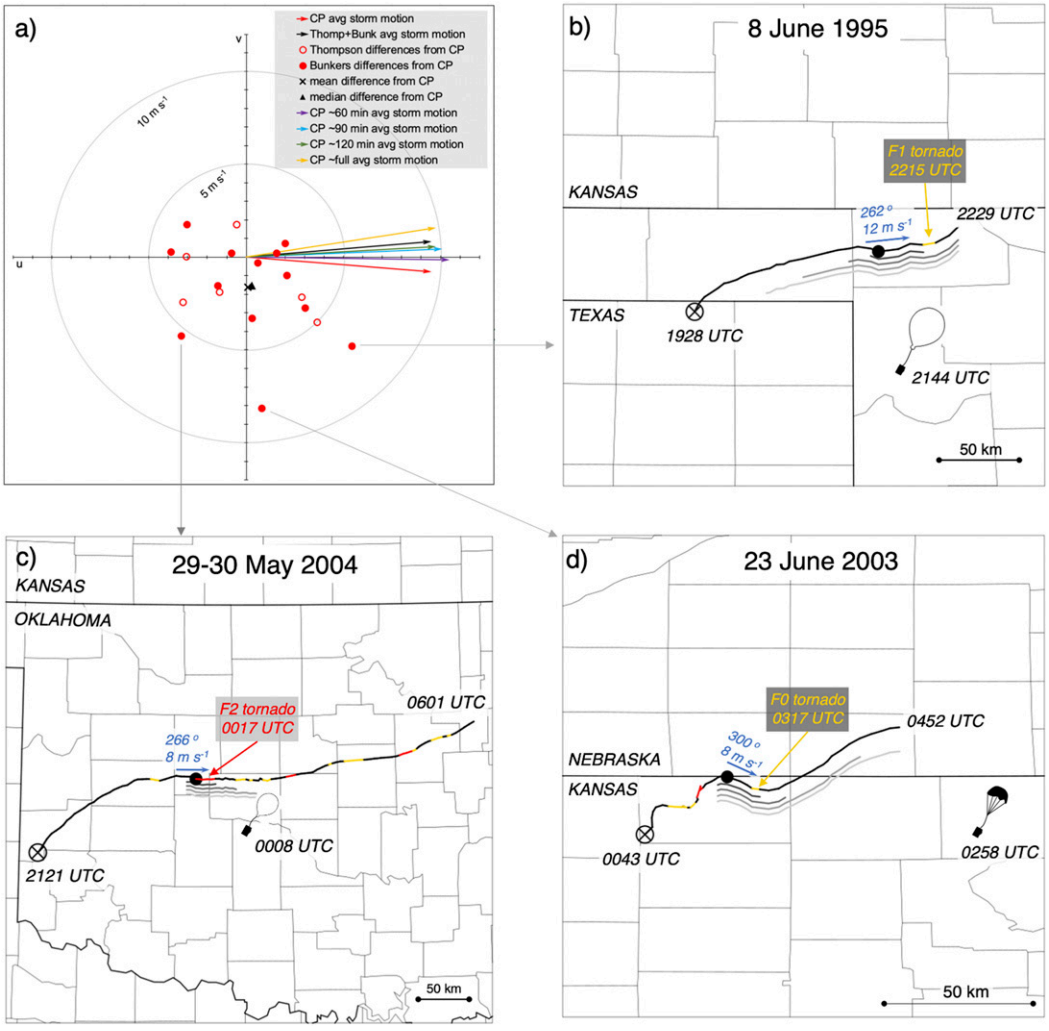

FIG. 5. (a) Comparison of 19 storm motions from cases common to the present study and two past datasets (see text for details). Wind-component differences (open and filled red circles) are computed from the storm motion estimates used in the present study (labeled "CP" in the legend). The mean and median of these differences are shown with the black × and triangle, respectively. Also shown are the storm motions averaged for the two past datasets (black arrow) and the present study (red arrow), along with storm motion estimates from the present study using longer averaging periods indicated in the legend (purple, blue, green, and gold arrows). (b),(c),(d) Illustrations of individual cases with the largest differences. Shown are the manually identified storm tracks in the present study (black lines), including the start and end times of the track, with the presence and start time of tornadoes along the track indicated by gold (≤F1) and red (≥F2). The time and location of the sonde used for the comparison are shown along with the location of the storm at the time of the sounding (filled black circle along the track). The approximate storm motion assigned to the sonde is shown in blue. Gray lines adjacent to the track indicate the different periods used to influence the storm-motion averages shown in (a) with the shortest gray line used for the red arrow in (a), which exemplifies a typical period used throughout this study.

mean critical angles (see "CA0100," "CA0250," and "CA0500" on Fig. 8). While the near-ground SRH is larger for the tornadic subset (Fig. 8), the larger SRH results from the larger shear and storm-relative wind rather than from different critical angles. As discussed in section 2 and shown later, it is important to consider the location of the soundings relative to the storm when describing critical angles, but in this comparison there is no appreciable difference in either the mean azimuth (see "AZI" in Fig. 8), or in the mean distance (see "DIST" in Fig. 8) of the two subsets. The lack of significant differences in mean critical angles does not discredit studies that show how near-ground streamwise vorticity resulting from critical angles closer to 90° might favor tornadogenesis in a given event (e.g., Esterheld and Giuliano 2008; Coffer and Parker 2017). Furthermore, the mean critical angles are 105°–125°, which are closer to 90° than 180° or 0°, suggesting that both tornadic and nontornadic soundings still

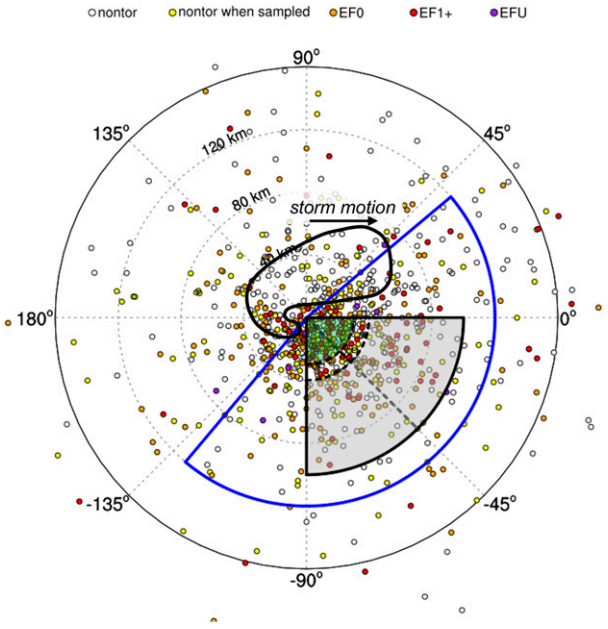

FIG. 6. Near-ground locations of each sounding relative to the updraft (at the origin) and storm motion (along the 0° azimuth). The presence of (or lack of) a tornado between 6 min prior to and 90 min after the time the sounding was near the ground is indicated by the colors of the dots (yellow indicates that the storm sampled by that sounding was tornadic at some point outside of the time window and no color fill indicates that storm was never tornadic). Soundings used in composite subsets for Figs. 8–13 are from the area enclosed by the blue line, and soundings used for Figs. 15–18 are within the quarter circle enclosed by the solid black line. Subsectors for the azimuth comparisons are separated by the dashed line at −45°. The near-field (far-field) soundings are taken from the area shaded in green (gray). An idealized outline of precipitation associated with a supercell is drawn for scale reference. Range rings are every 40 km.

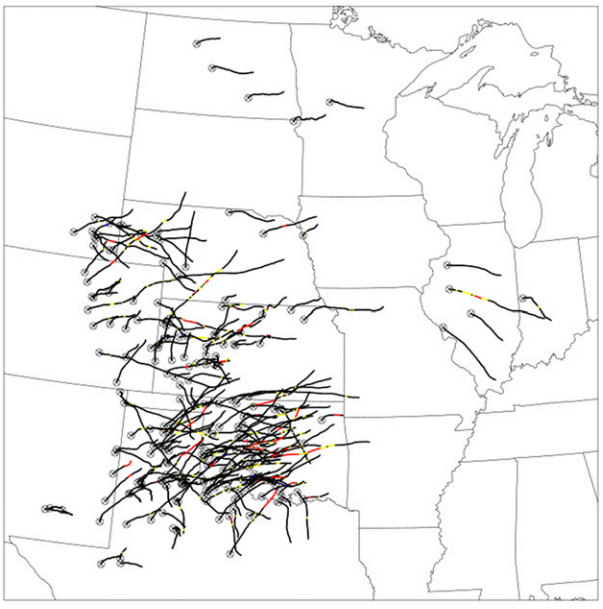

FIG. 7. Tracks of the 216 supercells sampled in this study starting from first echo (marked by ⊗) to when a supercell updraft could no longer be identified. The F/EF scale rating of tornadoes are indicated by colors: black = no tornado, yellow = EF0 or EF1, red = EF2+, and blue = EF unknown).

tend to have more streamwise than crosswise vorticity (additional analysis of the critical angle is provided later). Rather, as also shown in C19, these results suggest that *the critical angle may not be a robust discriminator between tornadic and nontornadic supercells*.

Another interesting finding that is revealed from the use of high-resolution soundings is *the low height at which hodograph curvature begins (i.e., the "kink"), which is near 250 m on average*. Among tornadic hodographs shown in past literature, heights are often plotted at intervals every 1 km, and only occasionally at 500 m intervals, probably because of coarse low-level data. This coarse labeling has made the height of the kink in many past studies ambiguous [a notable exception is Esterheld and Giuliano (2008) who show four examples of soundings with kinks between 200 and 250 m]. In this study, neither the mean height of the kink nor the critical angles vary substantially between the tornadic and nontornadic soundings, which suggests that the shear below the kink is a frictionally induced response to strong synoptically induced environmental inflow winds that exist in supercell environments regardless of the tornadic potential. Thus, the effects of friction acting on stronger ground-relative, near-ground winds below the kink likely contribute to the larger low-level shear and SRH for the tornadic environments.

Rather than the critical angle or the height of the hodograph kink, one of the strongest signals found in this study is the larger mean storm-relative winds at every level of the hodograph for the tornadic subset (Fig. 8). In fact, the variable with the largest difference among all tested is the mean 0–6 km v component of the storm-relative wind (VM06), for which the 95% confidence interval on the mean for the tornadic soundings is widely separated from that for the nontornadic soundings (Fig. 9). This difference in the mean results from a distribution of VM06 clearly shifted toward larger values for the tornadic soundings, for which values are almost never <0 and have many more instances of values $>15\ \mathrm{m\ s^{-1}}$ (Fig. 9). As described above, larger storm-relative winds contribute directly to larger SRH for a given shear magnitude and orientation. Beyond this direct role of increasing SRH, there are other possible influences of the storm-relative winds. Brooks et al. (1994) suggested that stronger storm-relative winds would favor stronger low-level mesocyclones by preventing excess evaporation and outflow-dominated storms. Some recent radar-based evidence of the importance of this mechanism may be seen in Crowe et al. (2012) who show that regions of enhanced K_{DP} and Z_{DR} within the storm are more separated within tornadic mesocyclones than nontornadic ones, indicating higher concentrations of small/medium raindrops farther away from the updraft. This separation distance between hydrometeors of different sizes (Kumjian and Ryzhkov 2012) is fundamentally a function of storm-relative

TABLE 3. Description of variables computed from the soundings that appear on Figs. 8–18.

Acronym	Meaning
ANG	Angle (°) between storm motion and azimuth of the sounding relative to the updraft (see Fig. 6 for the convention)
DIST	Distance (km) of the near-ground location of the sounding to the updraft
TIME	Time (UTC) of the sounding when near ground (launch time for upsondes, crash time for dropsondes)
CAPE##	Convective available potential energy ($J\,kg^{-1}$) using a lowest 100 hPa mixed parcel over the lowest 3 km (## = 03), the lowest 6 km (## = 06), and the lowest 10 km (## = 10)
MLCIN	Convective inhibition ($J\,kg^{-1}$) using a lowest 100 hPa mixed parcel
LR####	Temperature lapse rate ($°C\,km^{-1}$) over the lowest 100 m (#### = 0100), 250 m (#### = 0250), 500 m (#### = 0500), 1 km (#### = 01KM), 3 km (#### = 03KM), and 700–500 hPa (#### = 7500)
LLMIX	0–1 km mean mixing ratio ($g\,kg^{-1}$)
MLLCL	Lifting condensation level (m) using a lowest 100 hPa mixed parcel
GWS###	Ground-relative wind speed ($m\,s^{-1}$) at 10 m (## = 10), 250 m (### = 250), 500 m (### = 500), 1 km (### = 1KM), 2 km (### = 2KM), and 3 km (### = 3KM)
SWM####	Mean storm-relative wind speed ($m\,s^{-1}$) at 10 m (## = 10), 100 m (## = 100), 250 m (### = 250), 500 m (### = 500), 1 km (### = 1KM), and 6 km (### = 6KM)
SH####	Bulk wind difference ($m\,s^{-1}$) (vertical wind shear proxy) over the lowest 100 m (#### = 0100), 250 m (#### = 0250), 500 m (#### = 0500), 1 km (#### = 01KM) and 6 km (#### = 06KM)
CA####	Critical angle: Acute angle (°) between the 10 m storm-relative wind and the shear vector over the lowest 100 m (#### = 0100), 250 m (#### = 0250), 500 m (#### = 0500), and 1 km (#### = 01KM)
SRH####	Storm-relative helicity ($m^2\,s^{-2}$) between 100 m (#### = 0100), 250 m (#### = 0250), 500 m (#### = 0500), 1 km (#### = 01KM) and 3 km (#### = 03KM)
EFFSRH	Effective storm-relative helicity ($m^2\,s^{-2}$) (Thompson et al. 2007)
STP	Significant tornado parameter modified from Thompson et al. (2012) to use CAPE06 or CAPE10 when MLCAPE not available.

winds (Dawson et al. 2015). It is well known that evaporation rates and downdraft intensity increase with smaller drop size distributions (Srivastava 1987), so the stronger storm-relative winds for the tornadic soundings seen here may indicate the importance of keeping evaporatively chilled air away from the mesocyclone to increase the likelihood that it will be steady and long lived. Another possibility is that the stronger storm-relative winds help to maintain the strength of the parent supercell through its influence on supercell updraft width, maximum updraft speed, and maximum vertical vorticity (Peters et al. 2020).

The clear signal for larger low-level (<3 km) storm-relative winds is interesting because this was not found in a study of tornadic and nontornadic supercells by Markowski et al. (2003) and Thompson et al. (2003) (although those studies did find stronger storm-relative winds above ~3 km and stronger ground-relative winds up to 7 km in tornadic supercell environments). Like our study, they used observed storm motion and a large number of soundings (413). Potential differences arising from the different methods to compute storm motion are described in section 2. Furthermore, they pulled their sounding data from RUC analyses on 25 hPa levels but an exploration of potential errors from doing so await a future companion study. In the P14 and WCZ18 composites, storm-relative winds are slightly larger for the tornadic soundings (Fig. 1), but the differences between the tornadic and nontornadic subsets are not nearly as large as shown here. Interestingly, the largest differences in storm-relative winds in WCZ18 are seen near 2 km, similar to that shown in Fig. 8.

The stronger storm-relative winds for the tornadic subset result from a combination of larger ground-relative winds (see "GWS" variables in Fig. 7) and larger deviant storm motions [with some contribution from stronger deep-layer shear that increases the mean-wind component of the storm motion; Warren et al. 2017; Peters et al. 2019]. The storm motions for the tornadic subset are, on average, 19° to the right of the Bunkers motion estimates [using the original Bunkers et al. (2000) technique of using a non-pressure-weighted 0–6 km mean wind] versus 8° for the nontornadic subset (values for the observed and Bunkers motion vectors are given in the bottom right of the hodographs in Fig. 10). Bunkers (2018) also found tornadic supercells to deviate more than nontornadic supercells, although the differences are much smaller in that study (using a synoptic dataset). The differences in speed between the observed storm motion and Bunkers motion are only $0.4\,m\,s^{-1}$ for the nontornadic subset, but increase to $2.7\,m\,s^{-1}$ for the tornadic subset. The absolute errors—or magnitude of the difference vector between storm motion and the Bunkers estimates—are $5.0\,m\,s^{-1}$ for the tornadic subset and $1.4\,m\,s^{-1}$ for the nontornadic subset.[6] Because of these differences in deviant storm motions, the tornadic and nontornadic composite hodographs are more similar to one another when the hodographs are rotated with respect to the Bunkers et al. (2000) motion vectors (meaning the winds are rotated in coordinates with the Bunkers motion vector aligned with the x axis instead of the observed storm motion; Fig. 10b).

[6] Because direction deviations are not necessarily Galilean invariant, the deviations of the observed storm motion from Bunkers motion relative to the deep-layer shear vector were computed and were found to be consistent with these errors—the tornadic cases deviated $3.4\,m\,s^{-1}$ more to the right of the shear vector than the nontornadic cases.

TABLE 4. Sounding counts resulting from applying the criteria.

Criteria	Nontornadic	Tornadic	Total
None	597	305	902
−130° to 40° azimuth range	411	217	628
Above + no torcat = −1 in nontornadic subset	289	217	506
Above + distance ≤ 120 km	264	197	481
Above + CAPE03 > 0 and no outflow soundings	240	190	430

Note that the directional errors decrease to about 13° for the tornadic subset and 3° for the nontornadic subset when using the non-pressure-weighted 0–8 km mean wind as suggested in Ramsay and Doswell (2005), but the speed errors increase when doing so, up to 5 m s^{-1} too fast for the tornadic subset and 3 m s^{-1} too fast for the nontornadic subset. However, the accuracy of a particular hodograph-based method of estimating storm motion is less important here than 1) the changes in interpretation of storm–environment relationships when using observed storm motion versus a hodograph-based technique, and 2) the relationship between the differences in deviant motions for the tornadic and nontornadic subsets, which is preserved regardless of the technique used. In other words, the larger deviant motions found for the tornadic subset is not a function of how storm motion is prescribed [for a more complete description of how Bunkers motion estimates more generally relate to observed supercell motions, see Bunkers (2018)].

The above analysis shows that interpretations of storm–kinematic-environment relationships can depend on how storm motion is incorporated into the analysis. By using the observed storm motion instead of the original Bunkers motion technique, SRH03 and EFFSRH increase, SRH0500 and SRH01KM stay about the same, and SRH0100, and SRH0250 decrease slightly for the tornadic subsets (cf. Figs. 10a,b). For example, SRH03 increases from 333 to 418 m^2 s^{-2} for the tornadic subset but SRH0500 stays about 160 m^2 s^{-2}. Therefore, by using the observed storm motion instead of Bunkers motion, SRH integrated over 3 km increases primarily because of larger 1–3 km storm-relative winds (this is illustrated in Fig. 11). Empirical storm-motion estimates aside, supercells usually turn more to the right of the mean wind at some point in their evolution (three examples are shown in Fig. 5). If the hodograph stays fixed, Fig. 11 shows that as a storm turns more to the right, SRH03 is enhanced because of the contribution above ~1 km. Given that the tornadic supercells are found to directionally deviate more than twice as much to the right on average as their nontornadic counterparts, the tornadic supercells appear to benefit more from this boost in SRH above 500 m. If this boost in SRH and 1–3 km storm-relative wind arising from deviant motion plays a role in increasing the likelihood of tornadogenesis, then this suggests that processes related to low- to midlevel mesocyclone intensification or dispersed hydrometeors could be pushing the storm past a tipping point into a tornadic regime in these cases.

The reasons for the stronger deviant motions for the tornadic storms are not clear, but it is likely that larger initial vertical wind shear and SRH lead to stronger mesocyclones, and stronger dynamically induced updrafts and tilting that leads to stronger storm propagation away from the mean winds (i.e., a larger propagation component) (Weisman and Rotunno 2000; Davies-Jones 2002). A positive feedback may ensue, in which the larger propagation component leads to stronger storm-relative winds (as shown above), which in turn lead to even stronger updrafts (Peters et al. 2019) and further increases in SRH. Another possibility is discrete propagation owing to new cell development external to the storm, but the storm tracking procedure described above was designed to remove this potential factor. Three other possibilities for more deviant

TABLE 5. List of subset comparisons discussed in the text used to generate the mean soundings and hodographs. Definitions include the azimuth range (using the convention shown in Fig. 6), the distance range (km) from the updraft, the assigned nontornadic or tornadic category of the sounding (torcat), and the number of soundings, storms, and days in the subset. For the nontornadic and tornadic categories, numbers from 0 to 5 correspond to the F/EF rating of the tornado that occurred between 6 min prior to and 90 min after the radiosonde was near the ground, −2 corresponds to soundings that sampled a supercell that was never tornadic, and 9 corresponds to a rating of EF unknown. For all the below comparisons, only soundings for which CAPE03 > 0 are used.

	Comparison	Azimuth range (°)	Distance range (km)	torcat (s)	Soundings, storms, days
A	Nontornadic	−130 to 40	0 to 120	−2	240, 92, 66
	F/EF0+	−130 to 40	0 to 120	0 to 9	190, 75, 55
B	Nontornadic	−130 to 40	0 to 120	−2	240, 92, 66
	F/EF1+	−130 to 40	0 to 120	1 to 5	110, 44, 36
C	Nontornadic	−130 to 40	0 to 120	−2	240, 92, 66
	F/EF2+	−130 to 40	0 to 120	2 to 5	62, 25, 20
D	Nontornadic	−90 to −45	0 to 100	−2	64, 37, 31
	NONontornadicNTOR	−45 to 0	0 to 100	−2	73, 49, 46
E	F/EF0+	−90 to −45	0 to 100	0 to 9	59, 40, 35
	F/EF0+	−45 to 0	0 to 100	0 to 9	63, 41, 34
F	Nontornadic	−90 to 0	40 to 100	−2	69, 41, 37
	Nontornadic	−90 to 0	0 to 30	−2	41, 31, 26
G	F/EF0+	−90 to 0	40 to 120	0 to 9	63, 42, 34
	F/EF0+	−90 to 0	0 to 30	0 to 9	45, 30, 28

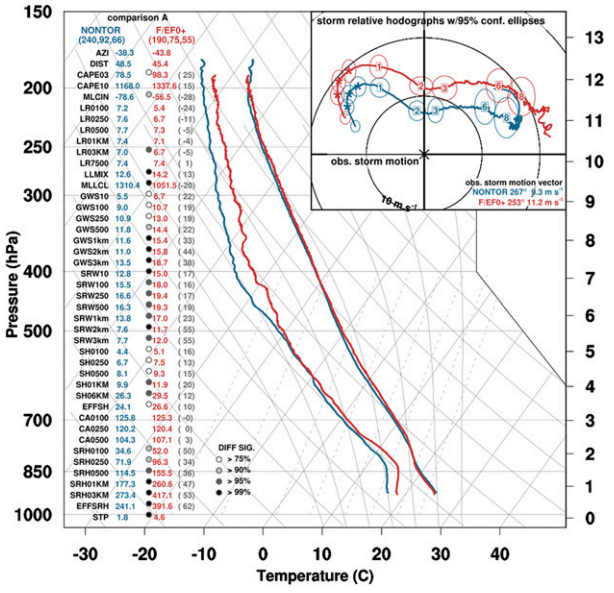

FIG. 8. Mean soundings, hodographs, and variables defined in Table 3 (means computed from individual soundings before averaging) for the nontornadic (blue) and F/EF0+ (red) subsets. The number of soundings, storms, and unique days in the subset, respectively, are shown in parentheses under the subset label in the top left. Statistical significance in the differences of the subset means is indicated by dots next to the values for the F/EF0+ subset and are shaded according to significance as shown. Numbers in gray in parentheses indicate the % change of the mean value for the F/EF0+ subset from that for the NONTOR subset. On the hodographs, asterisks are plotted at 100, 250, and 500 m AGL with height in km AGL indicated otherwise. Ellipses enclose the 95% confidence on the mean of the wind components. Wind components are remapped to coordinates with the observed storm motion at the origin prior to averaging with the mean ground-relative observed storm motion for each subset indicated on the bottom right of the hodograph. Range rings are every 10 m s^{-1}. Only those levels at which 50 or more sounding observations are available are displayed. Mean variables are not shown if either subset has <30 soundings with good data at levels required to compute the variable.

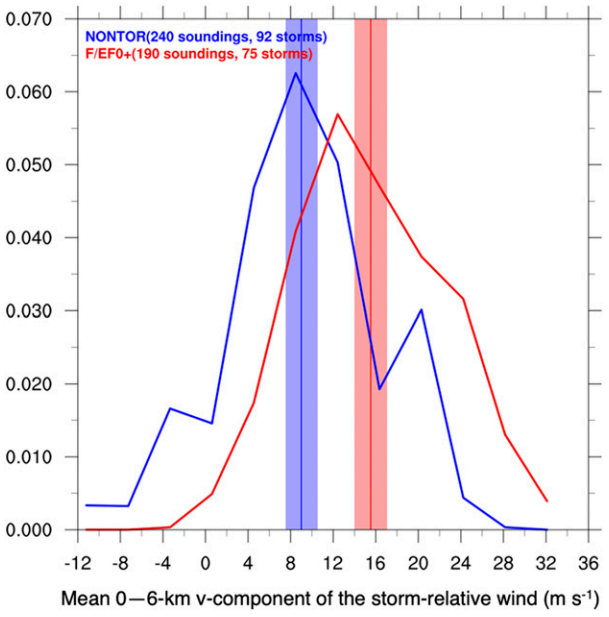

FIG. 9. Kernel density estimation of the mean 0–6 km v component of the storm-relative wind (m s^{-1}) for the F/EF0+ (red) and nontornadic (blue) soundings. Vertical lines indicate the mean, with the 95% confidence interval shaded around the mean.

storm motion are mentioned in Rasmussen and Blanchard (1998) and Bunkers et al. (2000): 1) stronger cold pools related to either high-precipitation storm modes or storms past their maturity, 2) the presence of mesoscale boundaries, and 3) terrain influences. None of these are obvious factors here; a survey of storm modes does not reveal a clear bias in mode or the life cycle stage sampled between the two subsets, the presence of obvious boundaries that influence storm motion were rare, and all of the storms were sufficiently removed from steep terrain.

Sensitivity to proximity criteria and inflow location

As described in section 2, it is important to explore how interpretations to Fig. 8 may change with changes in how proximity soundings are defined, which includes the location of the soundings relative to the updraft. Other than small increases in shear and storm-relative wind, no significant differences in interpretations from Fig. 8 are found by adding the torcat = −1 soundings to the nontornadic subset, using 80 or 160 km distance thresholds, using an azimuth range of −90° to 0°, or removing the CAPE03 > 0 requirement (not shown). However, some differences emerge when limiting the tornadic subset to stronger tornadoes and considering the location of the sounding in the inflow (choices for these subset definitions described next are summarized in Table 5).

1) F/EF-SCALE RATING

The primary differences seen in Fig. 8 amplify when using only the F/EF1+ tornado soundings (Fig. 12). Storm-relative winds increase at all levels, with complete separation of the 95% confidence ellipses on the wind components at every level up to 6 km. Differences in SRH increase, again resulting mostly from larger storm-relative wind and shear; the mean near-ground critical angles decrease only slightly toward 90° for the F/EF1+ soundings. Thermodynamically, the composite F/EF1+ sounding has more RH in the boundary layer than that for the F/EF0+ soundings resulting mostly from lower temperatures. Notably, compared to all tornadic storms, the F/EF1+ storms show a mean deviation even farther to the right of the mean Bunkers motion, which is 229° (not shown) compared to the mean observed motion of 251°—a difference of 22°.

Compared to the F/EF1+ subset, mean SRH values (and deviant motions) remain largely unchanged when only F/EF2+ soundings are used (Fig. 13). Subtle differences in the shape of the hodograph emerge near the ground, with the near-ground shear vectors veering slightly compared to those for the F/EF1+ events. However, the mean near-ground critical angles continue

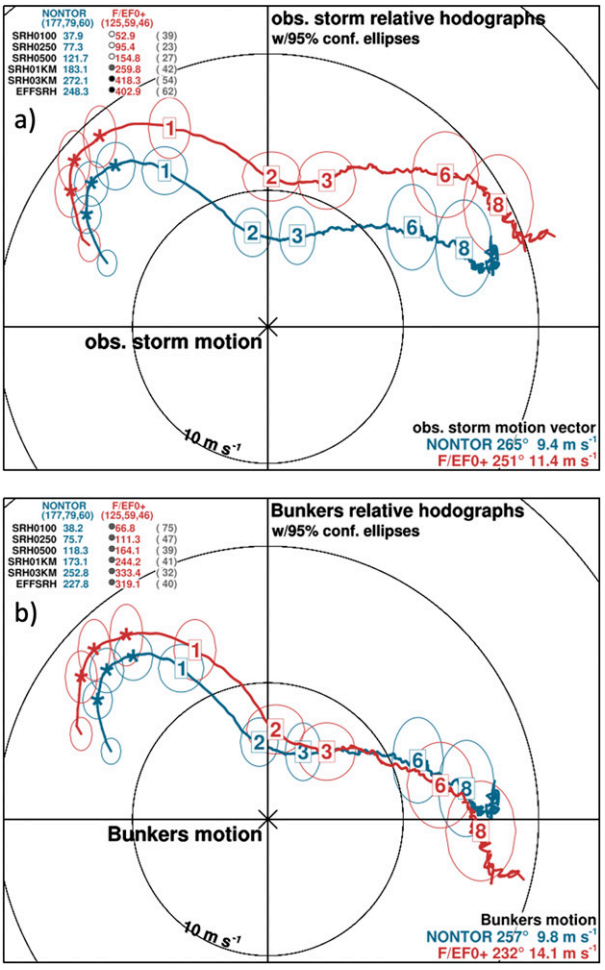

FIG. 10. (a) As in the hodograph in Fig. 8, but only for those soundings for which a Bunkers motion can be defined (note the smaller sample size compared to Fig. 8) and only mean values of SRH are shown. (b) As in (a), but the winds for the nontornadic and F/EF0+ subsets are rotated along the Bunkers motion prior to averaging. The absolute errors in Bunkers motion (magnitude of the difference vector between the Bunkers motion and storm motion) are 5.0 m s^{-1} for the tornadic soundings and 1.4 m s^{-1} for the nontornadic soundings.

to be statistically indistinguishable between the tornadic and nontornadic subsets (Fig. 13). C19 show that despite little difference in mean critical angles in their study, more angles are closer to 90° for significantly tornadic storms (see Fig. 3 in C19), and there is some signal of that result here for both the full tornadic (F/EF0+) set (Fig. 14a) and the F/EF1+ and F/EF2+ subsets (Figs. 14b,c), mostly for the angles <60°. However, a comparison of Figs. 14c and 3 of C19 shows a substantial difference between our studies; the mean CA0500 for the F/EF2 + soundings in this study is 106°, which falls well on the right side of the C19 distribution of significantly tornadic storms—the median critical angle is 63° in C19. The use of Bunkers motion in C19 versus the decidedly more rightward observed storm motion here explains only some of this difference; the mean CA0500 for

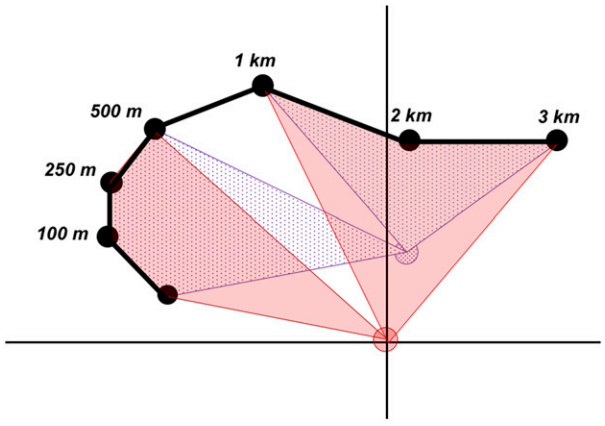

FIG. 11. Illustration of how SRH computed over 0–500 m and 1–3 km changes with a more rightward-deviant storm motion using the composite hodograph, observed storm motion (red shaded dot), and Bunkers motion (purple hatched dot) from the tornadic subset in Fig. 10. The red-shaded (purple-hatched) areas depict SRH computed over 0–500 m and 1–3 km resulting from the observed (Bunkers) storm motion.

the tornadic subset in this study decreases to 86°, and becomes significantly different than the CA500 for the nontornadic subset, when using Bunkers motion. Again, it is possible that low-level wind errors in the RUC/RAP soundings are a factor, but this will be explored in a future comparison of the present dataset to RUC/RAP profiles. Another possible factor is that C19 included many events from the Southeast United States whereas these are absent in our study.

2) AZIMUTH AND DISTANCE FROM THE UPDRAFT

To illustrate differences that arise as a function of azimuth, soundings are averaged within two sectors split evenly at −45° within the −90° to 0° sector shown in Fig. 6, called the southern and eastern sectors (a smaller distance and azimuth area is used here because it reduces differences in the mean distance between these two subsets). The low-level backing of the winds from the southern to the eastern sector seen from the P14 composite (Figs. 4a,b) also is seen here (Figs. 15 and 16) and is seen at all levels in the hodograph at which comparisons can be made. Notably, however, the conclusions about the importance of larger storm-relative winds for the tornadic soundings (cf. Figs. 15 and 16) is not a function of azimuth.

The dependencies on distance from the updraft are illustrated by averaging soundings in the near-field (0–30 km) and the far-field (40–100 km) from the −90° and 0° azimuths (see Fig. 6).[7] There is a signal for some low-level acceleration in the

[7] A 30 km distance is used in the near field to capture the slight differences in low-level hodographs in the nontornadic subsets shown in Fig. 17; otherwise the near-field and far-field nontornadic hodographs look nearly identical in low levels. As for the comparison of different azimuths, the −90° to 0° area is used here instead of the −130° to 40° area because it helps to reduce differences in azimuth between the near-field and far-field subsets.

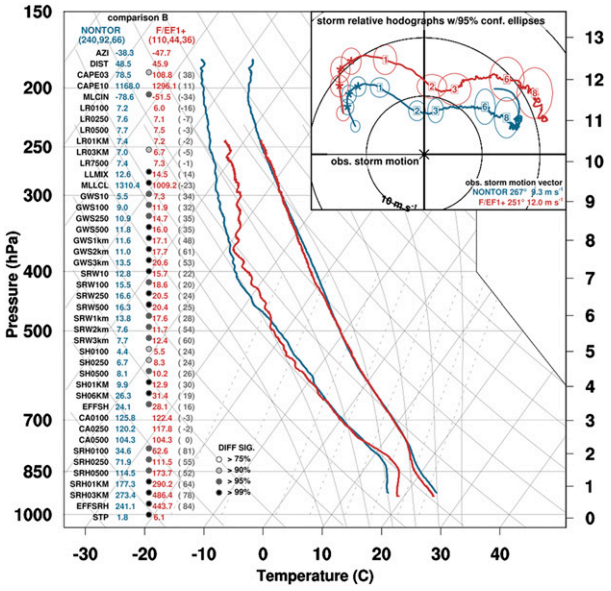

FIG. 12. As in Fig. 8, but only the F/EF1+ soundings are used for the tornadic subset.

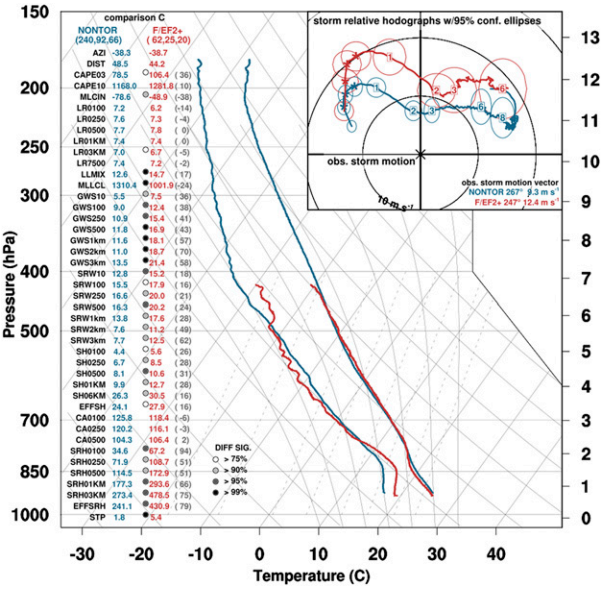

FIG. 13. As in Fig. 8, but only the F/EF2+ soundings are used for the tornadic subset and the minimum number of data points at each level is decreased to 30.

near-field of the storm, mostly for the tornadic soundings (Figs. 17 and 18). The noticeably larger accelerations noted for the tornadic soundings are an indication of larger low-level pressure deficits near the storm (evidence shown later points to this interpretation). To the extent that this lowered pressured is induced dynamically by stronger low-level rotation (evidence shown later also points to this interpretation), this is consistent with the interpretation that the more deviant rightward motions for the tornadic subset described earlier result from stronger mesocyclones. Furthermore, the smaller accelerations seen for the nontornadic soundings agree with WCZ18 that the near-field wind profile tends to be modified more by tornadic supercells than nontornadic ones, although the degree of modification shown here is not as large as in WCZ18, perhaps because the near- and far-fields were not sampled simultaneous for every storm here as in WCZ18. Also noteworthy is the substantial cooling/moistening above the boundary layer from the far-field to-near-field tornadic environment. WCZ18 found a similar result and show that this is likely a result of mesoscale lifting in the inflow, although evaporation of forward-flank precipitation cannot be ruled out as a factor. If this cooling/moistening is the result of lifting, it appears to be stronger for the tornadic storms, but it is not clear if this stronger lifting is a consequence of a stronger mesocyclone or stronger lifting in the background environment. Notably though, the cooling/moistening results in a thermodynamically favorable environment for sustaining convection by increasing CAPE03 and reducing MLCIN in the near-field environment (Figs. 17 and 18). SRH also is increased into the near-inflow as in WCZ18, but the significance of these increases are unknown given the reduction in effective sample sizes. Finally, the result of significantly stronger storm-relative winds for the tornadic subset (vs the nontornadic subset) in general does not change as a function of distance from the storm, just as this result did not change as a function of azimuth.

Similar to P14, the dependence of inflow characteristics on location in the inflow is explored further through a Barnes analysis (Barnes 1973, Koch et al. 1983) of the soundings (see appendix for details of the Barnes technique). The same criteria used to create Fig. 8 are used for the Barnes analyses shown in Fig. 19 so that poststorm and outflow soundings are not included; however, the distance requirement is removed to allow for all soundings in the −130° to 40° sector to be analyzed, which helps to fill in the analysis toward the edges of the domain. The analysis parameters are chosen to suppress localized storm-scale features but retain some amplitude of larger-scale heterogeneities across the inflow or mesoscale perturbations in the inflow that may be induced by the storm (see appendix for details). Dozens of variable–layer combinations were examined, but the most prominent differences in thermodynamic and kinematic variables are presented next.

As seen in Fig. 19, SRH03 is greater for the tornadic subset almost everywhere, but the largest differences are found in a corridor extending away from the updraft 90° to the right of the storm motion (‘‘south’’ in storm-relative terms) (Fig. 19c). Some of this increase closer to the updraft may be storm generated (e.g., near $x = -20$ km and between $y = 0$ and $y = -40$ km in Fig. 19c). However, there is an azimuthal gradient in SRH03 that exists well away from the updraft (e.g., the positive SRH03 differences decrease in magnitude as one follows constant range rings that are 40–80 km from the updraft from south to east in the inflow; Fig. 19c). Although storm modification to the SRH this far away from the storm cannot be ruled out, this suggests background environmental heterogeneity in SRH is present that is not seen for the nontornadic subset.

Another potentially important difference between the tornadic and nontornadic subsets is found in the low- to midlevel RH (Figs. 19d–f). The nontornadic subset shows little to no

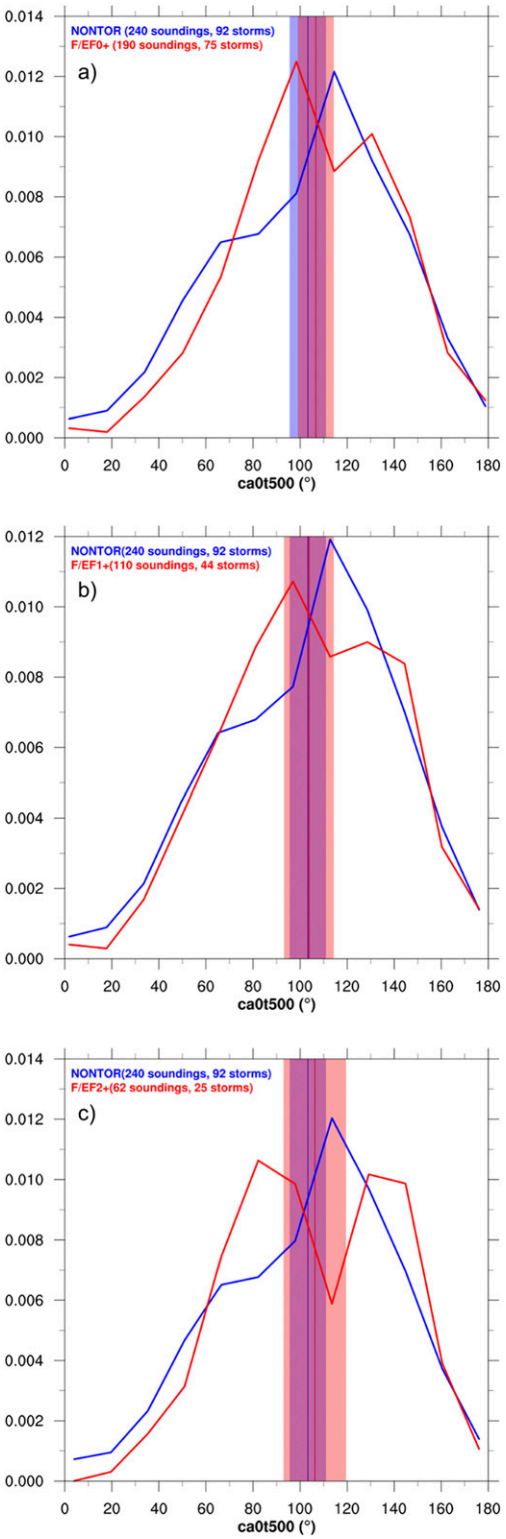

FIG. 14. Kernel density estimation of the 0–500 m critical angle (°) for the tornadic (red) and nontornadic (blue) soundings using the (a) F/EF0+, (b) F/EF1+, and (c) F/EF2+ tornadic subsets. Vertical lines indicate the mean, with the 95% confidence interval shaded around the mean.

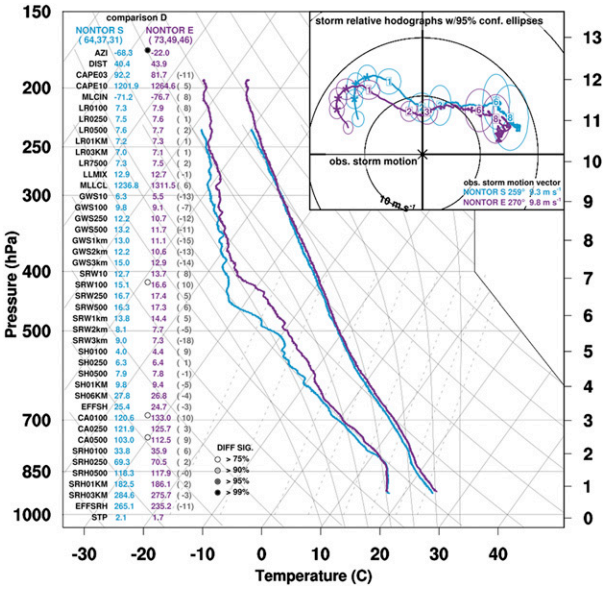

FIG. 15. As in Fig. 8, but only for the nontornadic soundings from azimuths between −90° and −45° (NONTOR S; blue) and −45° and 0° (NONTOR E; purple) and within 100 km of the updraft, and the minimum number of sounding points to compute an average is reduced to 30.

azimuthal gradient of 1–3 km mean RH in the inflow (Fig. 19e), but a corridor of relatively higher 1–3 km mean RH extends from the updraft to the south for the tornadic subset (Fig. 19d). This leads to analyzed 1–3 km RH that is 10%–15% higher in this corridor for the tornadic subset (from $y = 0$ to $y = -80$ km and $x = -20$ to $x = 20$ km in Fig. 19f). Some of this increase closer to the updraft could be from storm-induced lifting; but higher RH extends up to 80 km (and farther; not shown) from the updraft, suggesting higher 1–3 km mean RH exists in the background environment and could be the result of stronger meso- and synoptic-scale forcing for ascent for the tornadic subset. The southerly 2 km storm-relative winds in this corridor show that the higher RH is streaming into the updraft. This suggests two possible impacts, 1) that tornadic supercells suffer less from entrainment of subsaturated air into their low-level updrafts (Morrison 2017) than nontornadic supercells, and/or 2) for those cases in which the effective inflow layer (Thompson et al. 2007) extends above 1 km, more CAPE (or a deeper layer of CAPE) is being ingested into the right-flank of tornadic-supercell updrafts.

Finally, the possibility of a stronger mesocyclone for the tornadic soundings suggested earlier is explored further by producing a Barnes analysis of mean sea level pressure (MSLP) and low- to midlevel storm-relative winds. Because the features of interest here are potentially storm generated, soundings from all azimuths are used, outflow soundings are now included, and the CAPE03 > 0 requirement is removed (this allows for 417 nontornadic soundings and 305 tornadic soundings to be analyzed). Furthermore, the analysis parameters are modified to retain more meso-β amplitudes (see appendix). The most interesting feature seen in the MSLP analyses (Figs. 20a–c)

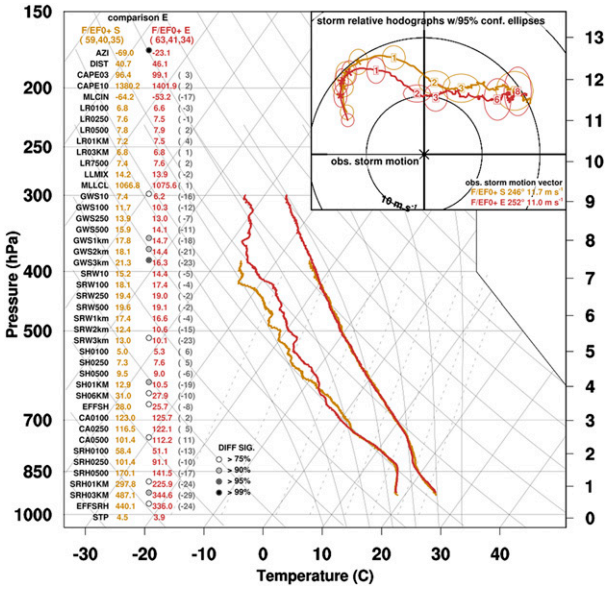

FIG. 16. As in Fig. 8, but only for the tornadic soundings from azimuths between −90° and −45° (F/EF0+ S) and −45° and 0° (F/EF0+ E) and within 100 km of the updraft, and the minimum number of sounding points to compute an average is reduced to 30.

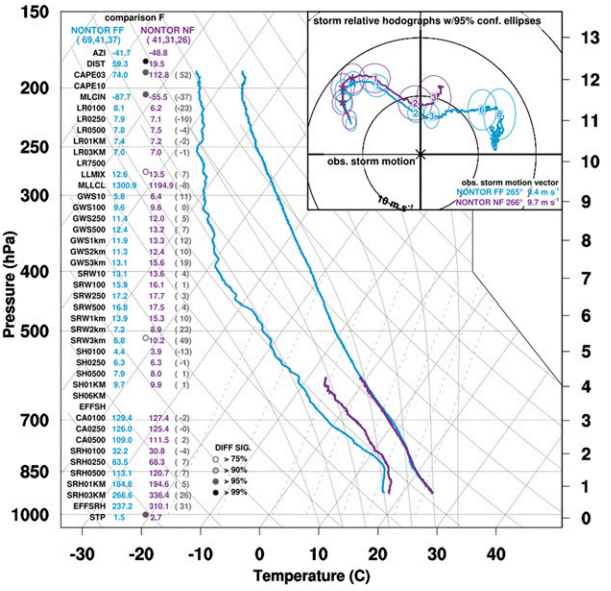

FIG. 17. As in Fig. 8, but only for the nontornadic far-field (NONTOR FF; blue) and nontornadic near-field (NONTOR NF; purple) subsets, and the minimum number of sounding points to compute an average is reduced to 25. Note that the composite near-field sounding stops at around 600 hPa because many of these soundings terminated early as they approached the storm.

is a meso-β-scale area of lower pressure under the updraft for the tornadic soundings (centered near the origin in Fig. 20c). This supports the idea discussed earlier that the tornadic supercells are inducing a significantly stronger perturbation low pressure than the nontornadic supercells, with a local minima in surface pressure near the updraft. Further evidence of this stronger mesocyclone is seen through analyses of storm-relative winds, which show a strong mesocyclonic flow response around the updraft, particularly from 2 to 4 km (shown for 3 km storm-relative winds in Fig. 20f). Therefore, *Fig. 20 provides direct observational evidence of the tendency for a stronger mesocyclone and associated surface pressure response underneath tornadic mesocyclones compared to nontornadic mesocyclones.* Past radar-based analyses have shown a positive relationship between rated tornado intensity and mesocyclone strength and lower tornado probabilities overall with weaker low-level storm rotation (e.g., Thompson et al. 2012, 2017). This study confirms these results, but solely from a collection of nearby sounding observations over many events, which underscores the influence that supercell mesocyclones have on their environment.

5. Summary and conclusions

A total of 902 extensively QC'ed soundings were compiled from field programs in the central United States and were related to nearby supercells through manual inspection of WSR-88D observations. Given the unique combination of a large dataset of observed proximity soundings with vertical resolution much higher than in RUC/RAP analyses or NWS-processed soundings, the goal of this study is to refine our knowledge of supercell environments, which includes an attempt to reconcile differences in conclusions from two recent studies (P14 and WCZ18).

By averaging and objectively analyzing proximity soundings, and exploring the sensitivity to sounding location and proximity criteria, the main findings can be summarized as follows:

- *Not surprisingly, the tornadic subset has significantly larger SRH than the nontornadic subset for all layers tested.* The larger SRH results from differences in storm-relative winds and vertical wind shear magnitude, not from differences in the critical angle. However, the tornadic soundings do show fewer critical angles <60° than the nontornadic soundings. There is substantial heterogeneity to the SRH differences in the inflow, with the largest differences found in a corridor extending away from the updraft ~90° to the right of the storm motion.
- *Differences seen in the critical angle in composite nontornadic hodographs soundings between the P14 and WCZ18 analyses likely result from sampling different locations in the inflow.* This provides motivation for future researchers to pay attention to the possible impacts of storm-relative position upon the critical angles depicted in their sounding datasets.
- *Stronger ground-relative winds and more rightward-deviant storm motions contributed to significantly larger storm-relative winds for the tornadic soundings.* The faster low-level storm-relative winds for the tornadic subset is somewhat surprising given the lack of a difference in storm-relative winds seen in other studies (e.g., Markowski et al. 2003; Thompson et al. 2003). Stronger storm-relative winds could be influencing tornado potential by contributing to 1) larger SRH, 2) a stronger updraft (Peters et al. 2020), and

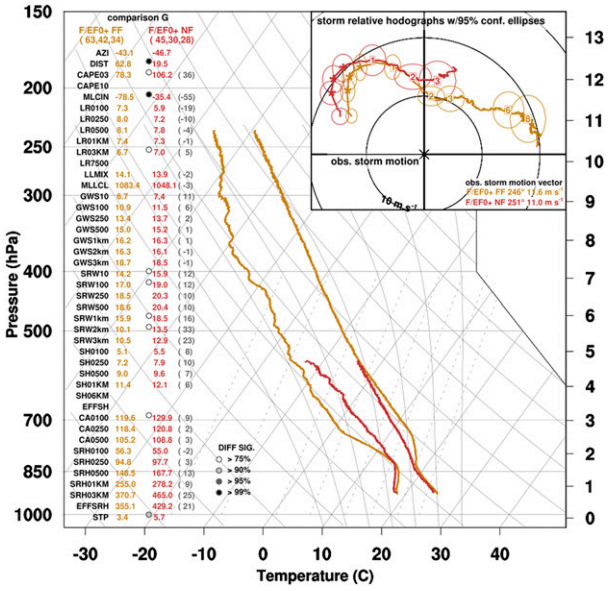

FIG. 18. As in Fig. 8, but only for the tornadic far-field (F/EF0+ FF; orange) and tornadic near-field (F/EF0+ NF; red) subsets, and the minimum number of sounding points to compute an average is reduced to 25. Note that the composite near-field sounding stops at around 600 hPa because many of these soundings terminated early as they approached the storm.

3) dispersing hydrometeors differently (Brooks et al. 1994; Kumjian and Ryzhkov 2012). Regarding the storm-relative wind contribution to SRH, assuming a fixed hodograph, the more rightward-deviant motions cause SRH to be enhanced aloft because of stronger 1–3 km storm-relative winds. Furthermore, the stronger 1–3 km storm-relative flow tends to advect air with higher RH into the updraft for the tornadic supercells, perhaps indicating that tornadic supercell updrafts suffer less from entrainment of subsaturated air (or are ingesting air with more CAPE in the upper portions of the effective inflow layer).

- *The tornadic mesocyclones appear to be significantly stronger on average than the nontornadic mesocyclones, which has not been shown before with an analysis of radiosonde observations.* Evidence includes a stronger response of the near-field low-level winds, a local minimum in surface mean sea level pressure differences analyzed underneath the updraft, and a clear mesoscale cyclonic response from the lower-tropospheric winds.
- *The hodograph "kink" (i.e., "the height at which hodograph curvature and stronger directional shear begins) is* ~250 m on average. The height of the kink in the present study, along with the critical angles below the kink, vary little between the tornadic and nontornadic soundings suggesting that the near-ground shear (that is mostly unidirectional) is a frictionally induced response to strong synoptically induced environmental inflow winds that exist in supercell environments regardless of the tornadic potential, but these inflow winds are substantially stronger in the tornadic subset.
- Similar to many past studies (e.g., Thompson et al. 2003; C19), *differences in thermodynamic variables between tornadic and nontornadic soundings are not as large as those found for the kinematic variables.* Some exceptions are 1) the expected lower MLLCLs and MLCIN related to higher low-level relative humidity in tornadic environments, 2) smaller 0–3 km lapse rates for the tornadic soundings related to weaker/shallower capping inversions in the far-field environment, and 3) larger 0–3 km CAPE in the near-field environments, related to cooling/moistening in the boundary layer.

In summary, the use of high vertical resolution targeted soundings to describe supercell environments provides much validation to supercell–environment relationships that have been established over many decades. Given a favorable thermodynamic environment, larger SRH, both near the ground and farther aloft, increases the likelihood of tornado production in supercells and that larger vertical wind shear is a primary cause. Where this study veers somewhat from past interpretations is the relative contributions to the SRH from the critical angle and storm-relative winds, the latter showing to be quite a robust difference in tornadic and nontornadic supercell soundings and the former, not so much. Significantly larger ground-relative winds are contributing to this difference in storm-relative winds, but perhaps not emphasized in past studies is the significantly larger rightward-deviant motions found for the tornadic supercells (likely related to the demonstrated stronger low- to midlevel mesocyclones), and furthermore, that this rightward-deviant motion tends to increase SRH above 1 km.

Although, anecdotally, forecasters and researchers have been aware of an increase in supercell intensity and organization with a rightward turn for some time, this has not been presented quantitatively from a large set of proximity soundings until this study. The relationships between tornadic supercells and storm-relative winds shown here suggest that being able to anticipate when a hard right turn will occur could provide a significant leap forward in tornado forecasting skill. Initial exploration into this problem is ongoing, but may be difficult to solve with this dataset because the subset sizes become small when considering only those soundings taken prior to the storms turning right. But emboldened by the importance of the storm-relative winds shown here, work will continue to attempt to understand this difficult forecast problem using the current and future datasets collected by TORUS and future supercell-related field projects.

Acknowledgments. The authors greatly appreciate helpful comments and suggestions from Matthew Flournoy, Erik Rasmussen, Clarice Satrio, Brice Coffer, Nicholas Goldacker, Levi Lovell, and Andy Wade that resulted in substantial improvements to the manuscript. Excellent formal reviews were provided by Matt Bunkers, Chris Nowotarski, and an anonymous reviewer. Radiosonde data used were obtained with support from multiple NOAA discretionary funding and National Science Foundation awards, including participation of the authors of this paper for VORTEX2 (AGS-1748715), MPEX (AGS-1230114), PECAN (AGS-1359726),

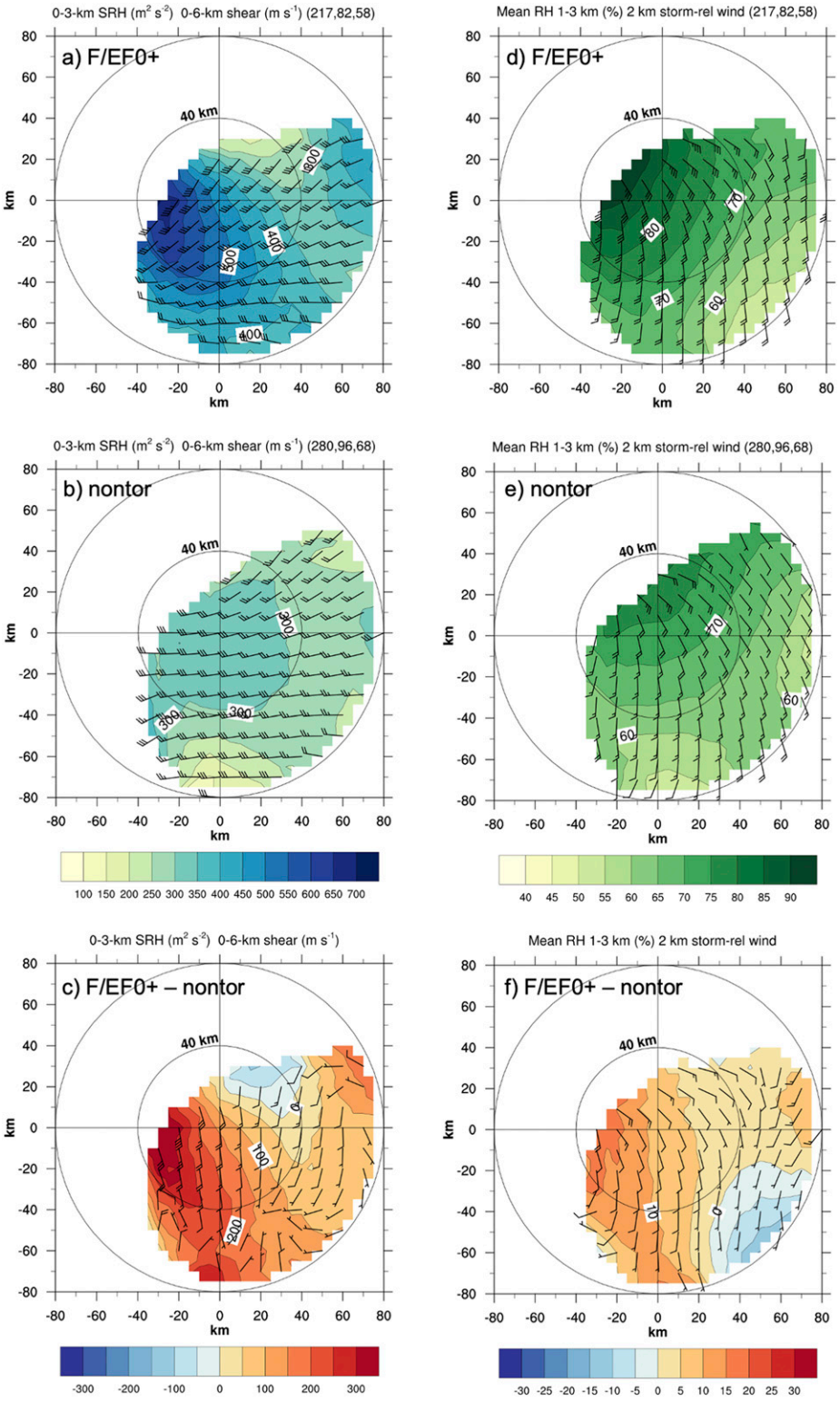

FIG. 19. (left) Barnes analysis of 0–3 km SRH and 0–6 km shear (half barb = 2.5 m s^{-1}, full barb = 5 m s^{-1}) for the (a) F/EF0+ and (b) nontornadic subsets. Soundings defined by comparison A in Table 5 are analyzed. SRH is contoured and shaded every 50 (m^2 s^{-2}) according to the color bar below (b). Numbers in parentheses in the titles indicate the number of soundings, storms, and days in the analysis. (c) Analysis differences (F/EF0+ minus nontornadic) contoured and shaded every 50 (m^2 s^{-2}) according

and TORUS (AGS-1824811). This project would not have been possible without the participation from hundreds of field project participants over the years including hundreds of students; we thank them for their tireless work. Plots were made using the NCAR command language (NCL), version 6.6.1.

Data availability statement. Most radiosonde data used during this study are openly available from the NCAR Earth Observing Laboratory Data Archive at https://data.eol.ucar.edu/. These data were reanalyzed by the first author. All of the data analyzed for this study and further information about data processing are available upon request from the National Severe Storms Laboratory through the first author (Michael.Coniglio@noaa.gov).

APPENDIX

Application of a Two-Pass Barnes Analysis on the Composite Data

The Barnes technique used here differs in a few ways from that used by P14. First, analyses of variables on constant height levels are not influenced by variables above or below, meaning the analysis for each variable is purely horizontal. Second, P14 only included cases for which enough soundings were taken to allow for a reference environment to be defined, from which perturbations of sounding variables were computed. The objective analysis was then performed on the perturbations prior to computation of sounding variables (e.g., CAPE and SRH). In this study, the analysis is performed on the full fields and, thus, variability in background (reference) environments is part of the analysis. A similar Barnes analysis using aggregated data were applied in Coniglio and Stensrud (2001) for producing a composite derecho environment, which included features seen in later composite derecho environments produced using alternative techniques (Coniglio et al. 2004; Guastini and Bosart 2016), thereby showing the efficacy of this technique for extracting features of the mesoscale environment.

A typical two-pass Barnes analysis creates a first-guess field for some variable f given by

$$f_0(i,j) = \frac{\sum_{n=1}^{N} w_n f_n(x,y)}{\sum_{n=1}^{N} w_n}, \tag{A1}$$

where the weighting w_n is given by

$$w_n = \exp\left(\frac{-d_n^2}{\kappa}\right), \tag{A2}$$

d_n is the distance from the (i, j) grid point to the observation $f_n(x, y)$, N is the number of data points chosen to influence the grid point within a radius R, and κ determines the wavelength dependent response of atmospheric structures in the first-guess field and is typically chosen with respect to the data spacing and representativeness. For this study κ is chosen to relate to R through $\kappa = 0.25 \times R^2$ so that w_n falls to ~0.02 for observations R km from the grid point. As in Barnes (1973), a second pass is used to force the first-guess field closer to the observations through the modified weight function:

$$w_n' = \exp\left(\frac{-d_n^2}{g\kappa}\right), \tag{A3}$$

where the final gridpoint values are determined by

$$f(i,j) = f_0(i,j) + \frac{\sum_{n=1}^{N} w_n' D_n}{\sum_{n=1}^{N} w_n'}, \tag{A4}$$

and

$$D_n = f_n(x,y) - f_0(x,y) \tag{A5}$$

is the difference between an observed data value and the estimated grid value obtained from the first-guess field at the same point.

Because the underlying data are an aggregation of soundings from different events, the analysis herein uses a value of κ much larger than typically would be used with data spacing as dense at that shown in the inflow environment in Fig. 6. Aggregating soundings from different cases presents an example of a representativeness concern discussed in Barnes (1973), for which he recommended using a large κ. Through much trial and error, values of $\kappa = 2500\,\text{km}^2$ (giving $R = 100$ km) and $g = 0.33$ were subjectively determined to provide an appropriate balance of resolving mesoscale features in the unmodified inflow environment while suppressing localized maxima and minima. Although the relevance of the theoretical response function of Barnes (1973) for this application is questionable given the aggregation of data from different cases and the wide variation in data spacing (Fig. 6), this choice of κ and g retains <1% of the amplitude of 40 km wavelength features, but retains nearly two-thirds the amplitude of 120 km wavelength features, respectively. While these parameters result in an analysis smoother than that shown in P14, these choices are appropriate because of the larger variability in the underlying data. Spurious maxima and minima were also mitigated by requiring at least 30 (N) observations within 100 km (R) of the grid point for the first pass, and at least 9 ($g \times N$) observations within 33 km ($g \times R$) of the grid point for the second pass; the analysis

←

to the color bar below (c). The updraft is at the origin and the storm motion is aligned with the x axis. Range rings are every 40 km. Only gridpoint values at which 30 soundings influence the analysis value are shown. (right) As in the left column, but only for the 1–3 km mean RH and 2 km storm-relative wind.

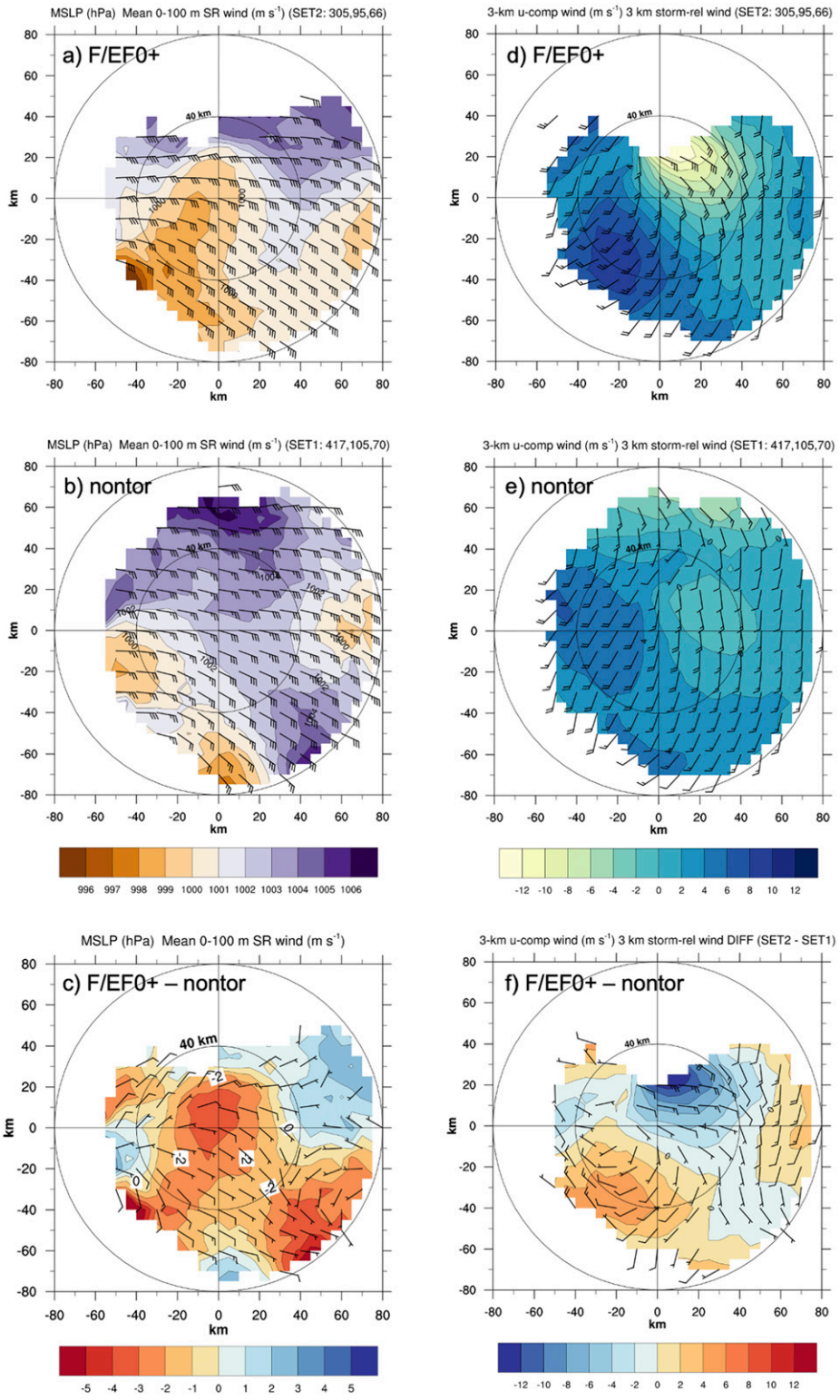

FIG. 20. As in Fig. 19, but only for the MSLP and mean 0–100 m storm-relative wind in the left column and 3 km u component of the storm-relative wind with the full 3 km storm-relative wind in barbs. Because absolute values of MSLP are less important here than MSLP gradients and mesoscale MSLP maxima/minima, 1.5 hPa is added to the tornadic subset in (b) (the approximate mean analysis-wide MSLP difference between the subsets) so that the mean MSLP is the same for both subsets.

is masked otherwise. The analysis at points outside of the azimuth thresholds (−130° and 40°) are masked to prevent aliasing of the analysis outside of locations occupied by the underlying data. Finally, for analyzing in-storm features for Fig. 20, an analysis to retain more mesoscale amplitudes is produced by using $\kappa = 1600\,\text{km}^2$ (giving $R = 80\,\text{km}$).

REFERENCES

Barnes, S. L., 1973: Mesoscale objective map analysis using weighted time series observations. NOAA Tech. Memo. ERL NSSL-62, 60 pp.

Beebe, R. G., 1958: Tornado proximity soundings. *Bull. Amer. Meteor. Soc.*, **39**, 195–201, https://doi.org/10.1175/1520-0477-39.4.195.

Benjamin, S. G., and Coauthors, 2016: A North American hourly assimilation and model forecast cycle: The Rapid Refresh. *Mon. Wea. Rev.*, **144**, 1669–1694, https://doi.org/10.1175/MWR-D-15-0242.1.

Brooks, H. E., and J. Correia Jr., 2018: Long-term performance metrics for National Weather Service tornado warnings. *Wea. Forecasting*, **33**, 1501–1511, https://doi.org/10.1175/WAF-D-18-0120.1.

——, C. A. Doswell III, and J. Cooper, 1994: On the environments of tornadic and nontornadic mesocyclones. *Wea. Forecasting*, **9**, 606–618, https://doi.org/10.1175/1520-0434(1994)009<0606:OTEOTA>2.0.CO;2.

Brotzge, J. A., S. E. Nelson, R. L. Thompson, and B. T. Smith, 2013: Tornado probability of detection and lead time as a function of convective mode and environmental parameters. *Wea. Forecasting*, **28**, 1261–1276, https://doi.org/10.1175/WAF-D-12-00119.1.

Browning, K. A., 1964: Airflow and precipitation trajectories within severe local storms which travel to the right of the winds. *J. Atmos. Sci.*, **21**, 634–639, https://doi.org/10.1175/1520-0469(1964)021<0634:AAPTWS>2.0.CO;2.

——, and F. Ludlam, 1962: Airflow in convective storms. *Quart. J. Roy. Meteor. Soc.*, **88**, 117–135, https://doi.org/10.1002/qj.49708837602.

Bunkers, M. J., 2018: Observations of right-moving supercell motion forecast errors. *Wea. Forecasting*, **33**, 145–159, https://doi.org/10.1175/WAF-D-17-0133.1.

——, B. A. Klimowski, J. W. Zeitler, R. L. Thompson, and M. L. Weisman, 2000: Predicting supercell motion using a new hodograph technique. *Wea. Forecasting*, **15**, 61–79, https://doi.org/10.1175/1520-0434(2000)015<0061:PSMUAN>2.0.CO;2.

——, D. A. Barber, R. L. Thompson, R. Edwards, and J. Garner, 2014: Choosing a universal mean wind for supercell motion prediction. *J. Oper. Meteor.*, **2**, 115–129, https://doi.org/10.15191/nwajom.2014.0211.

Ciesielski, P. E., P. T. Haertel, R. H. Johnson, J. Wang, and S. M. Loehrer, 2012: Developing high-quality field program sounding datasets. *Bull. Amer. Meteor. Soc.*, **93**, 325–336, https://doi.org/10.1175/BAMS-D-11-00091.1.

Coffer, B. E., and M. D. Parker, 2017: Simulated supercells in nontornadic and tornadic VORTEX2 environments. *Mon. Wea. Rev.*, **145**, 149–180, https://doi.org/10.1175/MWR-D-16-0226.1.

——, and ——, 2018: Is there a ''tipping point'' between simulated nontornadic and tornadic supercells in VORTEX2 environments? *Mon. Wea. Rev.*, **146**, 2667–2693, https://doi.org/10.1175/MWR-D-18-0050.1.

——, ——, R. L. Thompson, B. T. Smith, and R. E. Jewell, 2019: Using near-ground storm relative helicity in supercell tornado forecasting. *Wea. Forecasting*, **34**, 1417–1435, https://doi.org/10.1175/WAF-D-19-0115.1.

Coniglio, M. C., 2012: Verification of RUC 0–1-h forecasts and SPC mesoscale analyses using VORTEX2 soundings. *Wea. Forecasting*, **27**, 667–683, https://doi.org/10.1175/WAF-D-11-00096.1.

——, and D. J. Stensrud, 2001: Simulation of a progressive derecho using composite initial conditions. *Mon. Wea. Rev.*, **129**, 1593–1616, https://doi.org/10.1175/1520-0493(2001)129<1593:SOAPDU>2.0.CO;2.

——, ——, and M. B. Richman, 2004: An observational study of derecho-producing convective systems. *Wea. Forecasting*, **19**, 320–337, https://doi.org/10.1175/1520-0434(2004)019<0320:AOSODC>2.0.CO;2.

——, G. S. Romine, D. D. Turner, and R. D. Torn, 2019: Impacts of targeted AERI and Doppler lidar wind retrievals on short-term forecasts of the initiation and early evolution of thunderstorms. *Mon. Wea. Rev.*, **147**, 1149–1170, https://doi.org/10.1175/MWR-D-18-0351.1.

Craven, J. P., and Coauthors, 2004: Baseline climatology of sounding derived parameters associated with deep, moist convection. *Natl. Wea. Dig.*, **28**, 13–24.

Crowe, C. C., C. J. Schultz, M. Kumjian, L. D. Carey, and W. A. Petersen, 2012: Use of dual-polarization signatures in diagnosing tornadic potential. *Electron. J. Oper. Meteor.*, **13** (5), 57–78.

Darkow, G. L., 1969: An analysis of over sixty tornado proximity soundings. *Sixth Conf. on Severe Local Storms*, Chicago, IL, Amer. Meteor. Soc., 218–221.

Davies, J. M., and R. H. Johns, 1993: Some wind and instability parameters associated with strong and violent tornadoes: 1. Wind shear and helicity. *The Tornado: Its Structure, Dynamics, Prediction, and Hazards*, *Geophys. Monogr.*, Vol. 79, Amer. Geophys. Union, 573–582.

Davies-Jones, R., 1984: Streamwise vorticity: The origin of updraft rotation in supercell storms. *J. Atmos. Sci.*, **41**, 2991–3006, https://doi.org/10.1175/1520-0469(1984)041<2991:SVTOOU>2.0.CO;2.

——, 2002: Linear and nonlinear propagation of supercell storms. *J. Atmos. Sci.*, **59**, 3178–3205, https://doi.org/10.1175/1520-0469(2003)059<3178:LANPOS>2.0.CO;2.

Dawson, D. T., E. R. Mansell, and M. R. Kumjian, 2015: Does wind shear cause hydrometeor size sorting? *J. Atmos. Sci.*, **72**, 340–348, https://doi.org/10.1175/JAS-D-14-0084.1.

Esterheld, J. M., and D. J. Giuliano, 2008: Discriminating between tornadic and non-tornadic supercells: A new hodograph technique. *Electron. J. Severe Storms Meteor.*, **3** (2), https://ejssm.org/ojs/index.php/ejssm/article/viewArticle/33.

Fawbush, E. J., and R. C. Miller, 1954: The types of airmasses in which North American tornadoes form. *Bull. Amer. Meteor. Soc.*, **35**, 154–165, https://doi.org/10.1175/1520-0477-35.4.154.

Gallo, B. T., A. J. Clark, and S. R. Dembek, 2016: Forecasting tornadoes using convection-permitting ensembles. *Wea. Forecasting*, **31**, 273–295, https://doi.org/10.1175/WAF-D-15-0134.1.

Guastini, C. T., and L. F. Bosart, 2016: Analysis of a progressive derecho climatology and associated formation environments. *Mon. Wea. Rev.*, **144**, 1363–1382, https://doi.org/10.1175/MWR-D-15-0256.1.

Hampshire, N. L., R. M. Mosier, T. M. Ryan, and D. E. Cavanaugh, 2018: Relationship of low-level instability and tornado damage rating based on observed soundings. *J. Oper. Meteor.*, **6**, 1–12, https://doi.org/10.15191/nwajom.2018.0601.

Hart, J. A., and A. E. Cohen, 2016: The statistical severe convective risk assessment model. *Wea. Forecasting*, **31**, 1697–1714, https://doi.org/10.1175/WAF-D-16-0004.1.

Ingleby, B., and Coauthors, 2016: Progress toward high-resolution, real-time radiosonde reports. *Bull. Amer. Meteor. Soc.*, **97**, 2149–2161, https://doi.org/10.1175/BAMS-D-15-00169.1.

Kerr, B. W., and G. L. Darkow, 1996: Storm-relative winds and helicity in the tornadic thunderstorm environment. *Wea. Forecasting*, **11**, 489–505, https://doi.org/10.1175/1520-0434(1996)011<0489:SRWAHI>2.0.CO;2.

Klees, A. M., Y. P. Richardson, P. M. Markowski, C. Weiss, J. M. Wurman, and K. K. Kosiba, 2016: Comparison of the tornadic and nontornadic supercells intercepted by VORTEX2 on 10 June 2010. *Mon. Wea. Rev.*, **144**, 3201–3231, https://doi.org/10.1175/MWR-D-15-0345.1.

Koch, S. E., M. DesJardins, and P. J. Kocin, 1983: An interactive Barnes objective map analysis scheme for use with satellite and conventional data. *J. Climate Appl. Meteor.*, **22**, 1487–1503, https://doi.org/10.1175/1520-0450(1983)022<1487:AIBOMA>2.0.CO;2.

Kumjian, M. R., and A. V. Ryzhkov, 2012: The impact of size sorting on the polarimetric radar variables. *J. Atmos. Sci.*, **69**, 2042–2060, https://doi.org/10.1175/JAS-D-11-0125.1.

Lawson, J. R., J. S. Kain, N. Yussouf, D. C. Dowell, D. M. Wheatley, K. H. Knopfmeier, and T. A. Jones, 2018: Advancing from convection-allowing NWP to warn-on-forecast: Evidence of progress. *Wea. Forecasting*, **33**, 599–607, https://doi.org/10.1175/WAF-D-17-0145.1.

Maddox, R. A., 1976: An evaluation of tornado proximity wind and stability data. *Mon. Wea. Rev.*, **104**, 133–142, https://doi.org/10.1175/1520-0493(1976)104<0133:AEOTPW>2.0.CO;2.

Markowski, P. M., and Y. P. Richardson, 2014: The influence of environmental low-level shear and cold pools on tornadogenesis: Insights from idealized simulations. *J. Atmos. Sci.*, **71**, 243–275, https://doi.org/10.1175/JAS-D-13-0159.1.

——, J. M. Straka, E. N. Rasmussen, and D. O. Blanchard, 1998: Variability of storm-relative helicity during VORTEX. *Mon. Wea. Rev.*, **126**, 2959–2971, https://doi.org/10.1175/1520-0493(1998)126<2959:VOSRHD>2.0.CO;2.

——, C. Hannon, J. Frame, E. Lancaster, A. Pietrycha, R. Edwards, and R. L. Thompson, 2003: Characteristics of vertical wind profiles near supercells obtained from the Rapid Update Cycle. *Wea. Forecasting*, **18**, 1262–1272, https://doi.org/10.1175/1520-0434(2003)018<1262:COVWPN>2.0.CO;2.

Morrison, H., 2017: An analytic description of the structure and evolution of growing deep cumulus updrafts. *J. Atmos. Sci.*, **74**, 809–834, https://doi.org/10.1175/JAS-D-16-0234.1.

Newton, C. W., 1960: Morphology of thunderstorms and hailstorms as affected by vertical wind shear. *Physics of Precipitation*,*Geophys. Monogr.*, Vol. 5, Amer. Geophys. Union, 339–347.

Nowotarski, C. J., and E. A. Jones, 2018: Multivariate self-organizing map approach to classifying supercell tornado environments using near-storm, low-level wind and thermodynamic profiles. *Wea. Forecasting*, **33**, 661–670, https://doi.org/10.1175/WAF-D-17-0189.1.

Parker, M. D., 2014: Composite VORTEX2 supercell environments from near-storm soundings. *Mon. Wea. Rev.*, **142**, 508–529, https://doi.org/10.1175/MWR-D-13-00167.1.

Passi, R. M., and C. Morel, 1987: Wind errors using the worldwide Loran network. *J. Atmos. Oceanic Technol.*, **4**, 690–700, https://doi.org/10.1175/1520-0426(1987)004<0690:WEUTWL>2.0.CO;2.

Peters, J. M., C. J. Nowotarski, and H. Morrison, 2019: The role of vertical wind shear in modulating maximum supercell updraft velocities. *J. Atmos. Sci.*, **76**, 3169–3189, https://doi.org/10.1175/JAS-D-19-0096.1.

——, ——, J. P. Mulholland, and R. L. Thompson, 2020: The influences of effective inflow layer streamwise vorticity and storm-relative flow on supercell updraft properties. *J. Atmos. Sci.*, **77**, 3033–3057, https://doi.org/10.1175/JAS-D-19-0355.1.

Potvin, C. K., K. L. Elmore, and S. J. Weiss, 2010: Assessing the impacts of proximity sounding criteria on the climatology of significant tornado environments. *Wea. Forecasting*, **25**, 921–930, https://doi.org/10.1175/2010WAF2222368.1.

Ramsay, H. A., and C. A. Doswell, 2005: A sensitivity study of hodograph-based methods for estimating supercell motion. *Wea. Forecasting*, **20**, 954–970, https://doi.org/10.1175/WAF889.1.

Rasmussen, E. N., 2003: Refined supercell and tornado forecast parameters. *Wea. Forecasting*, **18**, 530–535, https://doi.org/10.1175/1520-0434(2003)18<530:RSATFP>2.0.CO;2.

——, and D. O. Blanchard, 1998: A baseline climatology of sounding-derived supercell andtornado forecast parameters. *Wea. Forecasting*, **13**, 1148–1164, https://doi.org/10.1175/1520-0434(1998)013<1148:ABCOSD>2.0.CO;2.

Rust, W. D., D. W. Burgess, R. A. Maddox, L. C. Showell, T. C. Marshall, and D. K. Lauritsen, 1990: Testing a mobile version of a cross-chain Loran atmospheric (M-CLASS) chain sounding system. *Bull. Amer. Meteor. Soc.*, **71**, 173–180, https://doi.org/10.1175/1520-0477(1990)071<0173:TAMVOA>2.0.CO;2.

——, T. C. Marshall, M. Stolzenburg, and J. Fitzgibbon, 1999: Test of a GPS radiosonde in thunderstorm electrical environments. *J. Atmos. Oceanic Technol.*, **16**, 550–560, https://doi.org/10.1175/1520-0426(1999)016<0550:TOAGRI>2.0.CO;2.

Schaefer, J. T., and R. L. Livingston, 1988: The typical structure of tornado proximity soundings. *J. Geophys. Res.*, **93**, 5351–5364, https://doi.org/10.1029/JD093iD05p05351.

Sherburn, K. D., M. D. Parker, J. R. King, and G. M. Lackmann, 2016: Composite environments of severe and nonsevere high-shear, low-CAPE convective events. *Wea. Forecasting*, **31**, 1899–1927, https://doi.org/10.1175/WAF-D-16-0086.1.

Showalter, A. K., and J. R. Fulks, 1943: Preliminary report on tornadoes. U.S. Weather Bureau, 162 pp.

Smith, B. T., R. L. Thompson, J. S. Grams, C. Broyles, and H. E. Brooks, 2012: Convective modes for significant severe thunderstorms in the contiguous United States. Part I: Storm classification and climatology. *Wea. Forecasting*, **27**, 1114–1135, https://doi.org/10.1175/WAF-D-11-00115.1.

Srivastava, R., 1987: A model of intense downdrafts driven by the melting and evaporation of precipitation. *J. Atmos. Sci.*, **44**, 1752–1774, https://doi.org/10.1175/1520-0469(1987)044<1752:AMOIDD>2.0.CO;2.

Thompson, R. L., R. Edwards, J. A. Hart, K. L. Elmore, and P. Markowski, 2003: Close proximity soundings within supercell environments obtained from the Rapid Update Cycle. *Wea. Forecasting*, **18**, 1243–1261, https://doi.org/10.1175/1520-0434(2003)018<1243:CPSWSE>2.0.CO;2.

——, C. M. Mead, and R. Edwards, 2007: Effective storm-relative helicity and bulk shear in supercell thunderstorm environments. *Wea. Forecasting*, **22**, 102–115, https://doi.org/10.1175/WAF969.1.

——, B. T. Smith, J. S. Grams, A. R. Dean, and C. Broyles, 2012: Convective modes for significant severe thunderstorms in the contiguous United States. Part II: Supercell and QLCS tornado environments. *Wea. Forecasting*, **27**, 1136–1154, https://doi.org/10.1175/WAF-D-11-00116.1.

——, and Coauthors, 2017: Tornado damage rating probabilities derived from WSR-88D data. *Wea. Forecasting*, **32**, 1509–1528, https://doi.org/10.1175/WAF-D-17-0004.1.

UCAR/NCAR/CISL/TDD, 2019: The NCAR Command Language (Version 6.6.1) [Software]. UCAR/NCAR/CISL/TDD, accessed 2019, http://doi.org/10.5065/D6WD3XH5.

Wade, A. R., M. C. Coniglio, and C. L. Ziegler, 2018: Comparison of near- and far-field supercell inflow environments using radiosonde observations. *Mon. Wea. Rev.*, **146**, 2403–2415, https://doi.org/10.1175/MWR-D-17-0276.1.

Wang, J., H. L. Cole, D. J. Carlson, E. R. Miller, K. Beierle, A. Paukkunen, and T. K. Laine, 2002: Corrections of humidity measurement errors from the Vaisala RS80 radiosonde—Application to TOGA COARE data. *J. Atmos. Oceanic Technol.*, **19**, 981–1002, https://doi.org/10.1175/1520-0426(2002)019<0981:COHMEF>2.0.CO;2.

Warren, R. A., H. Richter, H. A. Ramsay, S. T. Siems, and M. J. Manton, 2017: Impact of variations in upper-level shear on simulated supercells. *Mon. Wea. Rev.*, **145**, 2659–2681, https://doi.org/10.1175/MWR-D-16-0412.1.

Weisman, M. L., and R. Rotunno, 2000: The use of vertical wind shear versus helicity in interpreting supercell dynamics. *J. Atmos. Sci.*, **57**, 1452–1472, https://doi.org/10.1175/1520-0469(2000)057<1452:TUOVWS>2.0.CO;2.